

# A Unified-Field Monolithic Fictitious Domain-Finite Element Method for Fluid-Structure-Contact Interactions and Applications to Deterministic Lateral Displacement Problems

Cheng Wang<sup>a</sup>, Pengtao Sun<sup>b,\*</sup>, Yumiao Zhang<sup>e</sup>, Jinchao Xu<sup>c,d</sup>, Yan Chen<sup>e</sup>, Jiarui Han<sup>e</sup>

<sup>a</sup>*School of Mathematical Sciences, Tongji University, 1239 Siping Road, Shanghai 200092, China*

<sup>b</sup>*Department of Mathematical Sciences, University of Nevada Las Vegas, 4505 Maryland Parkway, Las Vegas, NV 89154, USA*

<sup>c</sup>*Department of Mathematics, Pennsylvania State University, University Park, PA 16802, USA*

<sup>d</sup>*Computer, Electrical and Mathematical Science and Engineering Division, King Abdullah University of Science and Technology, Thuwal 23955, Saudi Arabia*

<sup>e</sup>*Shenzhen Raymind Biotechnology Co., Ltd, 4018 Jintian Road, Shenzhen, China*

---

## Abstract

Based upon two overlapped, body-unfitted meshes, a type of unified-field monolithic fictitious domain-finite element method (UFMFD-FEM) is developed in this paper for moving interface problems of dynamic fluid-structure interactions (FSI) accompanying with high-contrast physical coefficients across the interface and contacting collisions between the structure and fluidic channel wall when the structure is immersed in the fluid. In particular, the proposed novel numerical method consists of a monolithic, stabilized mixed finite element method within the frame of fictitious domain/immersed boundary method (IBM) for generic fluid-structure-contact interaction (FSCI) problems in the Eulerian–updated Lagrangian description, while involving the no-slip type of interface conditions on the fluid-structure interface, and the repulsive contact force on the structural surface when the immersed structure contacts the fluidic channel wall. The developed UFMFD-FEM for FSI or FSCI problems can deal with the structural motion with large rotational and translational displacements and/or large deformation in an accurate and efficient fashion, which are first validated by two benchmark FSI problems and one FSCI model problem, then by experimental results of a realistic FSCI scenario – the microfluidic deterministic lateral displacement (DLD) problem that is applied to isolate circulating tumor cells (CTCs) from blood cells in the blood fluid through a cascaded filter DLD microchip in practice, where a particulate fluid with the pillar obstacles effect in the fluidic channel, i.e., the effects of fluid-structure interaction and structure collision, play significant roles to sort particles (cells) of different sizes with tilted pillar arrays. The developed unified-field, monolithic fictitious domain-based mixed finite element method can be seamlessly extended to more sophisticated, high dimensional FSCI problems with contacting collisions between the moving elastic structure and fluidic channel wall.

**Keywords:** Fluid-structure-contact interactions (FSCI), interface conditions, repulsive contact force, unified-field monolithic fictitious domain-finite element method (UFMFD-FEM), mixed finite element, deterministic lateral displacement (DLD).

**2020 MSC:** 65M22, 65M60, 65M85, 65Z05, 65D17, 70F35, 70F40, 74S05, 74F10, 76M10, 76M30, 76D05, 76D09

---

\*Corresponding author

*Email addresses:* wangcheng@tongji.edu.cn (Cheng Wang), pengtao.sun@unlv.edu (Pengtao Sun), yumiao.zhang@raymind.com (Yumiao Zhang), xu@math.psu.edu (Jinchao Xu), jinchao.xu@kaust.edu.sa (Jinchao Xu), yanc@raymind.com (Yan Chen), han@raymind.com (Jiarui Han)

# 1. Introduction

The interaction of a flexible structure with a flowing fluid it is submersed in or surrounded by gives rise to a rich variety of physical phenomena with applications in many fields of engineering and biology, e.g., the vibration of turbine blades impacted by the fluid flow, the response of bridges and tall buildings to winds, the floating parachute wafted by the air current, the rotating mechanical parts of percussive drill tool driven by the pressurized liquid, the flow of blood through the heart and arteries, the artificial heart pump and the intravascular stent, and etc. These examples comprise many applications of fluid-structure interaction (FSI) problems in hydrodynamics, aerodynamics and hemodynamics [61, 52, 9, 11, 36, 46, 34]. Figure 1 shows schematic domains of FSI in two cases. To understand the phenomena of FSI problems, it is necessary to find an effective way to model and simulate both the fluid motion and structural motion in a monolithic fashion by investigating the interactional mechanism between them. In general, FSI problems require the fluid and structure fields at the common interface to share not only the same velocity but also the common normal stress. There are currently two major numerical approaches classified by how the treatment of interface conditions of FSI and the fluid mesh are handled along the moving interface.

The first major approach is called the arbitrary Lagrangian Eulerian (ALE) technique [61, 19, 24, 22, 38, 49, 20, 27], which adapts the fluid mesh to accommodate the deformations of the structure on the interface and produces a body-fitted conforming mesh. Thus, interface conditions can be naturally satisfied within an interface location-dependent finite element space and its variational formulation. However, if the structure motion involves large deformations/displacements, then fluid elements tend to become ill-shaped, and accuracy loss will be imminent. This is commonly fixed with re-meshing techniques. However, the re-meshing process could be complicated, time consuming, and inaccurate. The transfer of solutions from the degenerated mesh to the new mesh may also introduce artificial diffusions, causing further inaccuracy. Moreover, the worst thing of the re-meshing process is that it breaks the mesh connectivity property of ALE mapping along the time which is crucial to carry out an optimal convergence analysis for ALE-based finite element methods.

Therefore, when the most advanced and best cultured ALE-based scheme inevitably reaches the point where only re-meshing helps, one might be tempted to turn over to the body-unfitted mesh method that leads to the second major approach – the fictitious domain method, which adopts the non-conforming mesh by extending the fluid from its domain  $\Omega_f^t$  to the interior structural domain  $\Omega_s^t$ , simultaneously, adding force-equivalent terms to the fluid equation as a representation of the interactional mechanism of the fluid and structure. Thus, re-meshing the fluid domain is avoided even for the case of large structural displacements/deformations. As shown in the right of Figure 1, the fictitious domain method requires two overlapped, body-unfitted meshes, in which one is the background fixed (Eulerian) fluid mesh, and the other one is the foreground moving (Lagrangian) structural mesh. A noticeable contribution to this approach

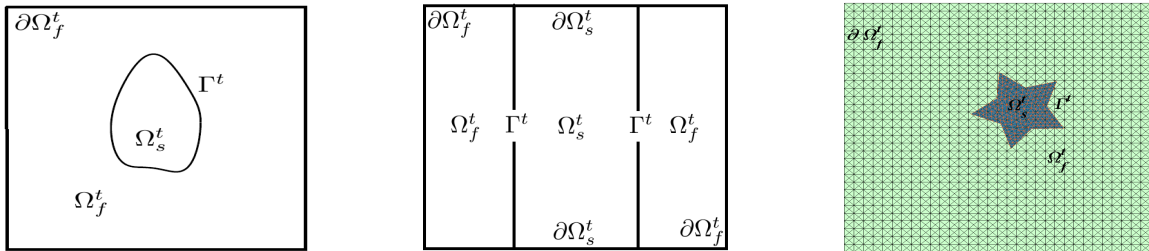


Figure 1: Illustrations of **(Left:)** the immersed case of FSI; **(Middle:)** the back-to-back case of FSI; **(Right:)** two overlapped, body-unfitted meshes.

is the immersed boundary method (IBM) [43, 44] for the structures that do not occupy volumes [28, 29, 53]. This introduces a pseudo delta function for communications between Eulerian and Lagrangian quantities. To accurately represent the interaction between a fluid and a bulk structure described by detailed constitutive laws, the extended IBM (EIBM) [64, 31, 32, 65, 66, 58, 60] was developed. In this method, a fictitious fluid is introduced to cover the structure domain and thus the fluid is extended to the entire domain. To enforce the interface conditions, the FSI force

is imposed not only on the fluid-structure interface as the IBM does, but also on every grid node in the fictitious fluid through a pseudo delta function. The fluid equations are then solved to yield the velocity field throughout the entire domain, afterwards, the structural (velocity/displacement) variables are gained through an interpolation process from the fluid mesh to the structural mesh. The obtained structural variables can then be substituted into the suitable structural constitutive law to update the FSI force, which in turn can be used by the fluid equation to find the new velocity of the fluid nodes, and so forth. Note that the IBM/EIBM is a semi-explicit finite difference scheme within a partitioned approach due to the explicit coupling between the fluid and the structure, therefore this method can be error-prone and may have stability problems, especially when the time step size is relatively large. Moreover, the involvement of a global Dirac delta distribution makes the analyses of well-posedness, stability and convergence properties even more difficult for IBM/EIBM.

To conquer those numerical deficiencies of IBM/EIBM, a fully implicit monolithic immersed domain approach has been developed with the help of the Lagrange multiplier, named the distributed Lagrange multiplier/fictitious domain (DLM/FD) method [14, 15, 63, 62, 47], which has recently gained considerable popularity in the simulation of interface problems including FSI [6, 3, 5, 55]. Same with the EIBM, the DLM/FD method also needs to extend the fluid to the structure domain as the fictitious fluid. However, instead of a  $d$ -dimensional Dirac delta function used in the EIBM, the DLM/FD method introduces the Lagrange multiplier (a pseudo body force) to enforce the fictitious fluid inside the structure to deform as the structure by constraining the fluid and structural velocities equal to each other in the structural domain. This results in a monolithic system which is essentially a saddle-point problem in regard to the Lagrange multiplier and principle unknowns. Simultaneously, this also nests a subproblem of saddle-point type for fluid equations. Thus a nested saddle-point problem is formed by the DLM/FD method for FSI, for which numerical analysis has long been missing due to its complexity. Until recently, some efforts including the authors' achievements have been made on the analyses of the well-posedness, stability and convergence of the nested saddle-point problem associated with the DLM/FD method [5, 55, 35, 50, 51, 57, 56], which shows that the accuracy of DLM/FD finite element method is of first-order in  $L^2$  norm and half order in  $H^1$  norm for linear finite element approximation to interface problems with non-smooth solutions across the interface, at most. In summary, the aforementioned immersed/body-unfitted mesh methods have become increasingly popular in FSI simulations due to their efficiency, flexibility and capability on handling FSI problems with complex structure motion that involves a large deformation/displacement for which the ALE method usually fails, although they usually lack the resolution near the interface. In addition, these body-unfitted mesh methods solely rely on the helps of either Dirac delta function or Lagrange multiplier, so their limited convergence results also depend on the discretization accuracies of Dirac delta function/Lagrange multipliers to which a poor approximation will result in a bad convergence of fictitious domain method.

Recently, Wang et al. in [59] develop a one-field fictitious domain method without introducing the Lagrange multiplier to weakly constrain the fictitious fluid velocity equals the structural velocity in the structural domain, which are instead reinforced to equal each other in a strong sense. Inspired by their work, in this paper we propose a unified-field monolithic fictitious domain-finite element method (UFMFD-FEM) based upon the weak form of the presented FSCI model in Eulerian-updated Lagrangian description, while considering the structural collision effect between the structure and fluidic channel wall in the FSI scenario that has been not only a challenging but also an open problem so far in terms of the definition of contact conditions and the method of finding and exerting the repulsive contact force on the immersed structure, and etc. We demonstrate that the weak form of the developed fictitious domain method can derive an equivalent strong form by means of a  $d$ -dimensional global Dirac delta distribution function that can be discretized by the EIBM, directly, which illustrates that our proposed fictitious domain method is actually in a close relation with the classical EIBM but more beyond since we develop a monolithic mixed finite element method for the presented FSCI model within the frame of unified-field fictitious domain method, in contrast with the classical EIBM that is mostly discretized by finite difference scheme for the strong form of FSI model via the Dirac delta function. In our proposed UFMFD-FEM, neither the Dirac delta function nor the Lagrange multiplier is involved, instead, a unified variable pair of the velocity and the pressure are defined in the entire domain on the fixed fluid mesh nodes only, and are shared by both the fluid and structural equations, besides that all advantages of the original fictitious domain/IBM are inherited, such as the interface-unfitted and time-independent background fluid mesh, on the top of

which a moving structural mesh is updated all the time through the material/Lagrangian mapping. In the meanwhile, our proposed method can also effectively deal with structural collisions with the fluidic channel wall while coexisting with fluid-structure interactions by treating the repulsive contact force, which is solved through a nonlinear iteration process, as a traction force on the contacting surface of structure.

The proposed UFMFD-FEM will be validated by two benchmark FSI problems, i.e., the motion of neutrally buoyant circular cylinders (i) in simple shear flow; and (ii) in plane Poiseuille flow, where convergence properties of the developed UFMFD-FEM are also investigated. In addition, we will also apply the developed UFMFD-FEM to a self-defined FSCI model problem for an investigation of structural collision influence on the particle's migration, and eventually, to a realistic microfluidic deterministic lateral displacement (DLD) problem for numerically checking the DLD critical diameter by releasing particles of different size in the fluid flow through a cascaded filter DLD microchip. If the particle size is smaller than the critical diameter, then the particle is isolated from the main stream and moves down to the lower row of micro-posts in the zigzag mode, otherwise it travels in the bumping mode over the micro-posts array (the inner wall of fluidic channel), where besides interactions between the particle and the fluid, the collisions amongst the particle and the micro-posts array are also significant to the particle's migration, and further, to the particle's isolation. Numerical results of our method have good agreements with physical experiments on a realistic DLD microchip.

The structure of this paper is organized as follows. In Section 2, we present a general FSCI model with fluid-structure interface conditions and structural contact conditions. Then, weak formulations of the presented FSCI model in both Eulerian-updated Lagrangian and Eulerian-total Lagrangian forms are defined in Section 3, where an IBM-based strong form is also derived via Dirac delta function. We propose the UFMFD-FEM in Section 4, and corresponding numerical algorithms and implementations in Section 5. Numerical experiments are carried out to validate the developed numerical method in Section 6 through two benchmark FSI problems, one self-defined FSCI model problem, and one realistic FSCI problem occurring in a cascaded filter DLD microchip. Finally, the concluding remarks and future work are given in Section 7.

## 2. Model descriptions

Let  $\Omega$  denote an open bounded domain in  $\mathbb{R}^d$  with a polygonal boundary  $\partial\Omega$ . For all  $t \in [0, T]$  with  $T$  as the terminal time,  $\Omega$  always consists of two subdomains, the fluid domain  $\Omega_f^t$  and the structure domain  $\Omega_s^t$  with a polygonal boundary  $\partial\Omega_s^t$ , which are separated by the fluid-structure interface  $\Gamma^t$  and satisfy  $\Omega = \Omega_f^t \cup \Omega_s^t$ ,  $\Omega_f^t \cap \Omega_s^t = \emptyset$ ,  $\Gamma^t = \partial\Omega_f^t \cap \partial\Omega_s^t$ . As shown in Figure 2, the structure domain  $\Omega_s^t$  can be considered as an image of a reference

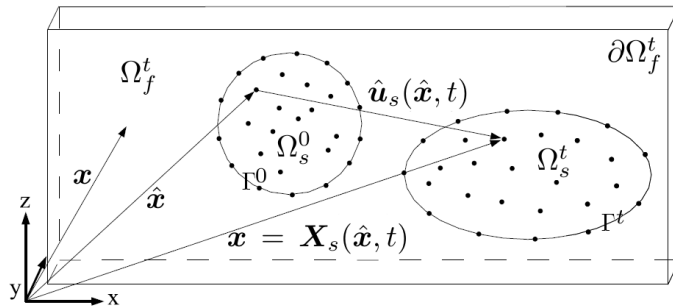


Figure 2: A schematic domain of FSI.

(initial/Lagrangian) domain  $\Omega_s^0$  via a family of material/Lagrangian mapping  $\mathbf{X}_s(t) : \Omega_s^0 \rightarrow \Omega_s^t$  defined as  $\mathbf{x} = \mathbf{X}_s(\hat{\mathbf{x}}, t)$  for all  $t \in [0, T]$ , which is associated with the material (Lagrangian) coordinate of points  $\hat{\mathbf{x}} \in \Omega_s^0$  and corresponding spatial (Eulerian) coordinate  $\mathbf{x} \in \Omega_s^t$ . Using  $\hat{\mathbf{u}}_s(\hat{\mathbf{x}}, t)$  to denote the structural displacement defined in  $\Omega_s^0$ , we attain a flow map,  $\mathbf{x} = \hat{\mathbf{x}} + \hat{\mathbf{u}}_s$ . Correspondingly, we introduce the deformation gradient tensor of structure,  $\mathbf{F} = \nabla_{\hat{\mathbf{x}}}\mathbf{x} = \nabla_{\hat{\mathbf{x}}}\mathbf{X}_s(\hat{\mathbf{x}}, t) = \mathbf{I} + \nabla_{\hat{\mathbf{x}}}\hat{\mathbf{u}}_s$ , and the Jacobian  $J = \det(\mathbf{F})$ . In what follows, we may use “ $\hat{\cdot}$ ” to denote a

quantity “ $\cdot$ ” that is associated with the reference domain of structure,  $\Omega_s^0$ , without further explanation, and, we use  $(\phi, \tilde{\phi})_\Psi = \int_\Psi \phi \tilde{\phi} d\mathbf{x}$  and  $\langle \phi, \tilde{\phi} \rangle_{\partial\Psi} = \int_{\partial\Psi} \phi \tilde{\phi} ds$  to denote a  $L^2$  inner product inside a region  $\Psi \subset \mathbb{R}^d$  ( $d = 2, 3$ ) and on a  $(d - 1)$ -dimensional region  $\partial\Psi$ , respectively.

### 2.1. Fluid motion

The fluid motion is described by the following incompressible Navier-Stokes equations with respect to the fluid velocity  $\mathbf{v}_f$  and the fluid pressure  $p_f$ ,

$$\begin{aligned} \rho_f \frac{D\mathbf{v}_f}{Dt} &= \nabla \cdot \boldsymbol{\sigma}_f + \rho_f \mathbf{g}, & \text{in } \Omega_f^t \times (0, T], \\ \nabla \cdot \mathbf{v}_f &= 0, & \text{in } \Omega_f^t \times (0, T], \end{aligned} \quad (1)$$

where the stress tensor  $\boldsymbol{\sigma}_f$  takes the form,  $\boldsymbol{\sigma}_f = -p_f \mathbf{I} + 2\mu_f \mathbf{D}(\mathbf{v}_f)$ , the rate-of-strain tensor  $\mathbf{D}(\mathbf{v}_f) = \frac{\nabla \mathbf{v}_f + (\nabla \mathbf{v}_f)^T}{2}$ ,  $\rho_f$ ,  $\mu_f$  denote the density and dynamic viscosity of the fluid, respectively,  $\frac{D}{Dt}$  represents the material derivative as  $\frac{D\mathbf{v}_f}{Dt} = \frac{\partial \mathbf{v}_f}{\partial t} + \mathbf{v}_f \cdot \nabla \mathbf{v}_f$ , and  $\mathbf{g}$  is the acceleration due to gravity. (1) subjects to the following Dirichlet boundary condition on the partial boundary  $\partial\Omega_{f,D}^t$ , the possible Neumann boundary condition on the rest boundary  $\partial\Omega_{f,N}^t$ , as well as the initial condition,

$$\begin{aligned} \mathbf{v}_f &= \mathbf{v}_{f,D}, & \text{on } \partial\Omega_{f,D}^t \times [0, T], \\ \boldsymbol{\sigma}_f \mathbf{n}_{f,N} &= \mathbf{f}_{f,N}, & \text{on } \partial\Omega_{f,N}^t \times [0, T], \\ \mathbf{v}_f(\mathbf{x}, 0) &= \mathbf{v}_f^0, & \text{in } \Omega_f^0, \end{aligned} \quad (2)$$

where  $\mathbf{n}_{f,N}$  is the outward normal unit vector on  $\partial\Omega_{f,N}^t$ . Additionally, in the scenario of FSI problems, other than (2), the fluid equation (1) shall also subject to the interface conditions defined in (5) across the interface of fluid and structure,  $\Gamma^t$ . In this case,  $\partial\Omega_f^t := \partial\Omega_{f,D}^t \cup \partial\Omega_{f,N}^t \cup \Gamma^t$ , for all  $t \in [0, T]$ .

### 2.2. Structure motion

We consider an incompressible structure material which is, for instance, always adopted to model the artery wall or blood cells in hemodynamic applications, and its dynamics is defined below in terms of the structural velocity  $\mathbf{v}_s$  and the structural (hydrostatic) pressure  $p_s$ ,

$$\begin{aligned} \rho_s \frac{D\mathbf{v}_s}{Dt} &= \nabla \cdot \boldsymbol{\sigma}_s + \rho_s \mathbf{g}, & \text{in } \Omega_s^t \times (0, T], \\ \nabla \cdot \mathbf{v}_s &= 0, & \text{in } \Omega_s^t \times (0, T], \end{aligned} \quad (3)$$

where  $\rho_s$  is the structural density,  $\boldsymbol{\sigma}_s$  denotes the Cauchy stress tensor of an incompressible hyperelastic structure. For instance, if an incompressible neo-Hookean (INH) material is adopted for the structure, then  $\boldsymbol{\sigma}_s = -p_s \mathbf{I} + \boldsymbol{\tau}_s$ , and  $\boldsymbol{\tau}_s = \mu_s (\mathbf{F}\mathbf{F}^T - \mathbf{I})$  is the deviatoric stress, here  $\mu_s$  is the shear modulus. Further, the structural hydrostatic pressure,  $p_s$ , plays a role of Lagrange multiplier to reinforce the incompressibility condition of structure,  $J = 1$  or  $\nabla \cdot \mathbf{v}_s = 0$ , mathematically [2, 18]. And, the structural velocity  $\mathbf{v}_s(\mathbf{x}, t) = \hat{\mathbf{v}}_s(\hat{\mathbf{x}}, t) = \frac{\partial \mathbf{X}_s}{\partial t}(\hat{\mathbf{x}}, t) = \frac{\partial \hat{\mathbf{u}}_s}{\partial t}$ . Thus,  $\frac{D\mathbf{v}_s}{Dt} = \frac{\partial^2 \mathbf{X}_s}{\partial t^2}(\hat{\mathbf{x}}, t)$  in Lagrangian description.

The following Dirichlet boundary condition and initial condition can be defined for (3),

$$\begin{aligned} \mathbf{v}_s &= \mathbf{v}_{s,D}, & \text{on } \partial\Omega_s^t \setminus \Gamma^t \times [0, T], \\ \mathbf{v}_s(\mathbf{x}, 0) &= \mathbf{v}_s^0, & \text{in } \Omega_s^0, \end{aligned} \quad (4)$$

which apply to some scenarios of FSI, e.g., when the structure is not fully immersed in the fluid but owns a fixed outer boundary, as shown in the middle of Figure 1. Otherwise  $\Gamma^t = \partial\Omega_s^t$ , where if no collision occurs between the immersed structure and the fluidic channel wall (see the left of Figure 1), then the fluid-structure interface conditions (5) are applied instead.

**Remark 2.1.** For the aforementioned material/Lagrangian mapping  $\mathbf{X}_s(t) : \Omega_s^0 \rightarrow \Omega_s^t$ , we further assume that it fulfills the following conditions,  $\mathbf{X}_s(t) \in W^{1,\infty}(\Omega_s^0)$ ,  $\mathbf{X}_s(t)$  is one to one, and there exists a constant  $\alpha$  such that  $\|\mathbf{X}_s(\hat{\mathbf{x}}_1, t) - \mathbf{X}_s(\hat{\mathbf{x}}_2, t)\| \geq \alpha\|\hat{\mathbf{x}}_1 - \hat{\mathbf{x}}_2\|$  for all  $\hat{\mathbf{x}}_1, \hat{\mathbf{x}}_2 \in \Omega_s^0$  and  $t \in [0, T]$ . Note that this requirements imply that  $\mathbf{X}_s(t)$  is invertible with Lipschitz inverse, which in particular implies that  $\hat{\mathbf{v}}_s(\hat{\mathbf{x}}, t) \in H^1(\Omega_s^0)^d$  if and only if  $\mathbf{v}_s = \hat{\mathbf{v}}_s \circ \mathbf{X}_s^{-1}(t) \in H^1(\Omega_s^t)^d$  [13, 39].

### 2.3. Fluid-structure interface conditions

We consider the following no-slip type interface conditions that can be applied to most cases of FSI problems,

$$\begin{aligned} \mathbf{v}_f &= \mathbf{v}_s, & \text{on } \Gamma^t \times [0, T], \\ \boldsymbol{\sigma}_f \mathbf{n} &= \boldsymbol{\sigma}_s \mathbf{n}, & \text{on } \Gamma^t \times [0, T], \end{aligned} \quad (5)$$

which are called the kinematic and the dynamic lateral interface condition describing the continuity of velocity, and the continuity of normal stress, respectively, where and in what follows,  $\mathbf{n}$  is the outward normal unit vector on  $\partial\Omega_s^t \cap \Gamma^t$  pointing into the fluid domain from the structural domain.

### 2.4. Structural collision and contact conditions

When a moving structure, which is immersed inside the fluid flow, collides with the fixed wall of the fluidic channel  $\partial\Omega$ , the collision phenomenon happens and generates a repulsive contact force acting on the contacting surface  $\Gamma_C^t$  that is actually a part of the structural surface  $\partial\Omega_s^t$ . To describe the mathematical model of structural collision, we divide the structural boundary  $\partial\Omega_s^t := \Gamma^t$  into two parts:

$$\Gamma_C^t := \left\{ \mathbf{x} \in \partial\Omega_s^t : \mathbf{x} \notin \overset{\circ}{\Omega} \right\}, \quad (6)$$

$$\Gamma_I^t := \partial\Omega_s^t \setminus \Gamma_C^t, \quad (7)$$

where  $\overset{\circ}{\Omega}$  denotes the interior of  $\Omega$ . We note that  $\Gamma_C^t$  can also be defined as  $\Gamma_C^t := \partial\Omega_s^t \cap \partial\Omega$ . Thus, once  $\Gamma_C^t \neq \emptyset$  when the collision happens, we exert the contact force on this part of structural boundary. Hence, two types of structural boundary conditions can be raised as follows with respect to two parts of  $\partial\Omega_s^t := \Gamma_I^t \cup \Gamma_C^t$ , respectively, as illustrated in Figure 3.

1. On  $\Gamma_I^t$  where there is no collision, only the fluid-structure interface conditions (5) are applied, i.e.,

$$\mathbf{v}_f = \mathbf{v}_s, \quad \boldsymbol{\sigma}_f \mathbf{n} = \boldsymbol{\sigma}_s \mathbf{n}, \quad \text{on } \Gamma_I^t \times [0, T]. \quad (8)$$

2. On  $\Gamma_C^t$ , the collision occurs by holding the following complementary conditions that are similar with, e.g., [10],

$$-\sigma_{s,\mathbf{n}} \geq 0, \quad v_{s,\mathbf{n}} \leq 0, \quad \sigma_{s,\mathbf{n}} v_{s,\mathbf{n}} = 0, \quad \text{on } \Gamma_C^t \times [0, T], \quad (9)$$

$$\boldsymbol{\sigma}_{s,\boldsymbol{\tau}} = 0, \quad \text{on } \Gamma_C^t \times [0, T], \quad (10)$$

where  $\sigma_{s,\mathbf{n}} = \mathbf{n} \cdot \boldsymbol{\sigma}_s \mathbf{n}$ ,  $v_{s,\mathbf{n}} = \mathbf{v}_s \cdot \mathbf{n}$ ,  $\mathbf{v}_{s,\boldsymbol{\tau}} = \mathbf{v}_s - v_{s,\mathbf{n}} \mathbf{n}$  and  $\boldsymbol{\sigma}_{s,\boldsymbol{\tau}} = \boldsymbol{\sigma}_s \mathbf{n} - \sigma_{s,\mathbf{n}} \mathbf{n}$ .

Figure 3(b) illustrates a typical occurrence of the collision between the immersed structure and the wall of fluidic channel, All boundary/interface conditions with respect to the involved boundaries/interface illustrated in Figure 3 are further redescribed below.

1. On the fluidic channel wall  $\partial\Omega$ , the Dirichlet- and Neumann boundary conditions (2) are defined.
2. On the fluid-structure interface  $\Gamma^t$ , the interface conditions (5) are defined.

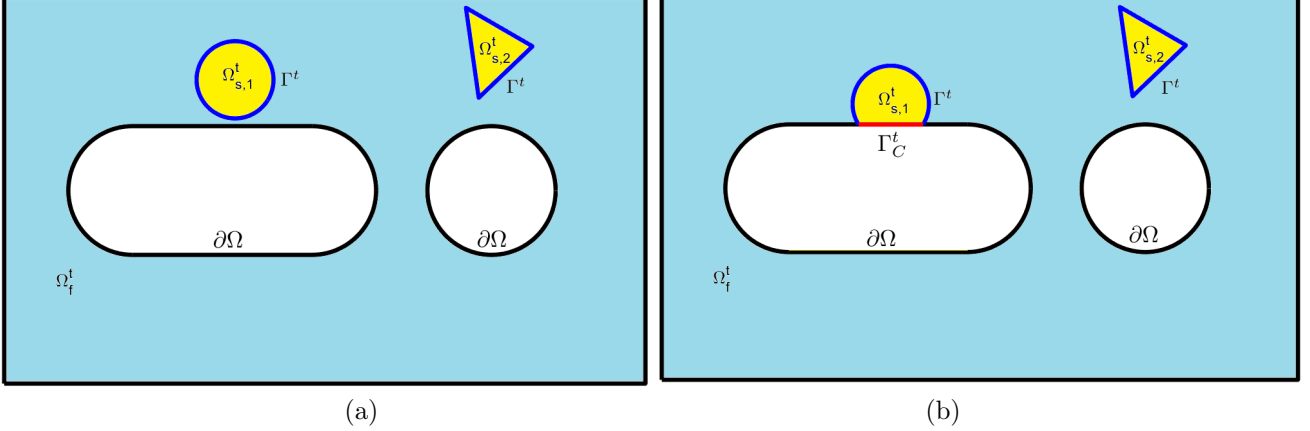


Figure 3: Schematic illustrations of two types of structural boundary conditions: (a) no collision occurs and thus interface conditions are applied to the (blue) fluid-structure interface  $\Gamma^t$ ; (b) the collision occurs and generates a repulsive contact force on the (red) contacting surface,  $\Gamma_C^t$ , between the structure and the fluidic channel wall, where the light blue area represents the fluid domain  $\Omega_f^t$ , the yellow areas are the immersed structures of different shapes,  $\Omega_s^t$ , and, the solid black lines denote the fluidic channel wall  $\partial\Omega$ .

3. On the contacting surface  $\Gamma_C^t$  where the structural collision occurs, the contact conditions (9) and (10) are applied. Note that in this case  $\Gamma_C^t$  is viewed as a part of structural boundary  $\partial\Omega_s^t$  that is neither a part of the fluidic channel wall  $\partial\Omega$  nor a part of the fluid-structure interface  $\Gamma^t$ . However, when no collision occurs,  $\Gamma_C^t$  vanishes and retreats back to  $\Gamma_I^t$  that is a part of  $\Gamma^t$  essentially, as illustrated in Figure 3(a).

By introducing a convex cone of admissible structural velocities which satisfy the non-interpenetration condition on the contact surface  $\Gamma_C^t$ , we might be able to obtain a weak form of the aforementioned FSCI model (1)-(5), (8)-(10), which is actually in the form of variational inequality by following an analogous derivation in [10, 30, 17]. However at this stage, we do not intend to prove the well-posedness of either this FSCI model or its relevant variational inequality that involve the complementary contact condition (9). In fact, the repulsive contact force on the contacting surface of structure  $\Gamma_C^t$  as well as  $\Gamma_C^t$  itself are not explicitly given in (9), which are actually determined by the entire nonlinear FSCI system in an implicit fashion. Inspired by similar arguments in [1, 48], we make the following assumption in this paper in order to process a successful numerical implementation later in Section 6 and a possible numerical analysis in the future.

**Assumption 1.** *The FSCI system (1)-(5) and (8)-(10) exists an unique solution, and, at any time when such a collision occurs, the contacting surface  $\Gamma_C^t$  and the repulsive contact force  $f_{s,C_W} := -\sigma_{s,n}$  exist, uniquely.*

Thus instead of (9), we can apply the following structural boundary condition on  $\Gamma_C^t$ ,

$$-\sigma_{s,n} = f_{s,C_W}, \quad \text{on } \Gamma_C^t \times [0, T], \quad (11)$$

which belongs to a Neumann-type of boundary condition. Therefore, for the FSCI system defined by (1)-(5), (8), (10) and (11), Assumption 1 implies that if we utilize the uniquely existing repulsive contact force  $f_{s,C_W}$  and the contact surface  $\Gamma_C^t$  in (10) and (11), then the solution of FSCI system (1)-(5), (8), (10) and (11) is also a solution of FSCI system (1)-(5) and (8)-(10), and thus still satisfies the complementary contact condition (9). Thus, we gain  $f_{s,C_W} \in [0, \infty)$ ,  $v_{s,n} \leq 0$  and  $\sigma_{s,n}v_{s,n} = 0$ , which will be used to design a nonlinear iteration process to determine  $f_{s,C_W}$  and  $\Gamma_C^t$  in the numerical implementation (see Algorithm 5.2).

### 3. Weak formulations

#### 3.1. Weak form of the fluid-structure-contact interaction model

Introduce the following notations of Sobolev spaces,

$$\begin{aligned}\widetilde{\mathbf{V}} &:= \{(\mathbf{v}_f, \mathbf{v}_s) \mid \mathbf{v}_f \in H^1(\Omega_f^t)^d, \mathbf{v}_s \in H^1(\Omega_s^t)^d; \mathbf{v}_f = \mathbf{v}_s \text{ on } \Gamma^t, \mathbf{v}_f = \mathbf{v}_{f,D} \text{ on } \partial\Omega_{f,D}^t, \mathbf{v}_s = \mathbf{v}_{s,D} \text{ on } \partial\Omega_s^t \setminus \Gamma^t\}, \\ \widetilde{\mathbf{V}}_0 &:= \{(\mathbf{v}_f, \mathbf{v}_s) \mid \mathbf{v}_f \in H^1(\Omega_f^t)^d, \mathbf{v}_s \in H^1(\Omega_s^t)^d; \mathbf{v}_f = \mathbf{v}_s \text{ on } \Gamma^t, \mathbf{v}_f = 0 \text{ on } \partial\Omega_{f,D}^t, \mathbf{v}_s = 0 \text{ on } \partial\Omega_s^t \setminus \Gamma^t\}, \\ \widetilde{W} &:= \{(p_f, p_s) \mid p_f \in L^2(\Omega_f^t), p_s \in L^2(\Omega_s^t)\},\end{aligned}\quad (12)$$

based on which we can derive a natural weak formulation of the dimensional FSCI model (1)-(5), (8), (10) and (11) as follows: for any  $[(\tilde{\mathbf{v}}_f, \tilde{\mathbf{v}}_s), (\tilde{p}_f, \tilde{p}_s)] \in \widetilde{\mathbf{V}}_0 \times \widetilde{W}$ , find  $[(\mathbf{v}_f, \mathbf{v}_s), (p_f, p_s)] \in H^1(0, T; \widetilde{\mathbf{V}}) \times L^2(0, T; \widetilde{W})$  such that

$$\begin{aligned}\left(\rho_f \frac{D\mathbf{v}_f}{Dt}, \tilde{\mathbf{v}}_f\right)_{\Omega_f^t} + 2(\mu_f \mathbf{D}(\mathbf{v}_f), \mathbf{D}(\tilde{\mathbf{v}}_f))_{\Omega_f^t} - (p_f, \nabla \cdot \tilde{\mathbf{v}}_f)_{\Omega_f^t} + \left(\rho_s \frac{D\mathbf{v}_s}{Dt}, \tilde{\mathbf{v}}_s\right)_{\Omega_s^t} + (\mu_s (\mathbf{F}\mathbf{F}^T - \mathbf{I}), \nabla \tilde{\mathbf{v}}_s)_{\Omega_s^t} \\ - (p_s, \nabla \cdot \tilde{\mathbf{v}}_s)_{\Omega_s^t} = (\rho_f \mathbf{g}, \tilde{\mathbf{v}}_f)_{\Omega_f^t} + (\rho_s \mathbf{g}, \tilde{\mathbf{v}}_s)_{\Omega_s^t} + \langle \mathbf{f}_{f,N}, \tilde{\mathbf{v}}_f \rangle_{\partial\Omega_{f,N}^t} - \langle f_{s,CW}, \tilde{\mathbf{v}}_s \cdot \mathbf{n} \rangle_{\Gamma_C^t},\end{aligned}\quad (13)$$

$$(\nabla \cdot \mathbf{v}_f, \tilde{p}_f)_{\Omega_f^t} + (\nabla \cdot \mathbf{v}_s, \tilde{p}_s)_{\Omega_s^t} = 0, \quad (14)$$

where the interface integral term vanishes from (13) due to the first interface condition (5)<sub>1</sub> that is built into the space  $\widetilde{\mathbf{V}}_0$  as well as the second interface condition (5)<sub>2</sub> when the integration by parts is applied to inner products of the fluidic and structural stress terms. Here the repulsive contact force  $f_{s,CW}$  and the contact surface  $\Gamma_C^t$  are implicitly determined by a nonlinear iteration algorithm as shown in Algorithm 5.2.

Because  $\Omega = \Omega_f^t \cup \Omega_s^t$  for all  $t \in [0, T]$ , by smoothly extending all fluid parts defined in  $\Omega_f^t$  into the structural domain  $\Omega_s^t$  as a kind of fictitious fluid while forcing the velocity to satisfy the interface condition (5)<sub>1</sub> not only on the interface  $\Gamma^t$  but also inside the entire structural domain,  $\dot{\Omega}_s^t$ , we can define the following Sobolev spaces of the unified velocity  $\mathbf{v}$  and unified pressure  $p$  in the entire domain  $\Omega$ , respectively,

$$\begin{aligned}\mathbf{V} &:= \{\mathbf{v} \in H^1(\Omega)^d \mid \mathbf{v}_f = \mathbf{v}|_{\Omega_f^t} \in H^1(\Omega_f^t)^d, \mathbf{v}_s = \mathbf{v}|_{\Omega_s^t} \in H^1(\Omega_s^t)^d; \mathbf{v} = \mathbf{v}_{f,D} \text{ on } \partial\Omega_{f,D}^t, \mathbf{v} = \mathbf{v}_{s,D} \text{ on } \partial\Omega_s^t \setminus \Gamma^t\}, \\ \mathbf{V}_0 &:= \{\mathbf{v} \in H^1(\Omega)^d \mid \mathbf{v}_f = \mathbf{v}|_{\Omega_f^t} \in H^1(\Omega_f^t)^d, \mathbf{v}_s = \mathbf{v}|_{\Omega_s^t} \in H^1(\Omega_s^t)^d; \mathbf{v} = 0 \text{ on } \partial\Omega_{f,D}^t \cup \partial\Omega_s^t \setminus \Gamma^t\}, \\ W &:= \{p \in L^2(\Omega) \mid p_f = p|_{\Omega_f^t} \in L^2(\Omega_f^t), p_s = p|_{\Omega_s^t} \in L^2(\Omega_s^t)\},\end{aligned}\quad (15)$$

utilizing which we are able to rewrite (13) and (14) as the following equivalent weak formulation in the fictitious domain frame, i.e., for any  $(\tilde{\mathbf{v}}, \tilde{p}) \in \mathbf{V}_0 \times W$ , find  $(\mathbf{v}, p) \in H^1(0, T; \mathbf{V}) \times L^2(0, T; W)$  such that

$$\begin{aligned}\left(\rho_f \frac{D\mathbf{v}}{Dt}, \tilde{\mathbf{v}}\right)_{\Omega} + 2(\mu_f \mathbf{D}(\mathbf{v}), \mathbf{D}(\tilde{\mathbf{v}}))_{\Omega} - (p, \nabla \cdot \tilde{\mathbf{v}})_{\Omega} + \left((\rho_s - \rho_f) \frac{D\mathbf{v}}{Dt}, \tilde{\mathbf{v}}\right)_{\Omega_s^t} + (\mu_s (\mathbf{F}\mathbf{F}^T - \mathbf{I}), \nabla \tilde{\mathbf{v}})_{\Omega_s^t} \\ - 2(\mu_f \mathbf{D}(\mathbf{v}), \mathbf{D}(\tilde{\mathbf{v}}))_{\Omega_s^t} = (\rho_f \mathbf{g}, \tilde{\mathbf{v}})_{\Omega} + ((\rho_s - \rho_f) \mathbf{g}, \tilde{\mathbf{v}})_{\Omega_s^t} + \langle \mathbf{f}_{f,N}, \tilde{\mathbf{v}} \rangle_{\partial\Omega_{f,N}^t} - \langle f_{s,CW}, \tilde{\mathbf{v}} \cdot \mathbf{n} \rangle_{\Gamma_C^t},\end{aligned}\quad (16)$$

$$(\nabla \cdot \mathbf{v}, \tilde{p})_{\Omega} = 0, \quad (17)$$

where all unified trial and test functions,  $\mathbf{v}$ ,  $p$ ,  $\tilde{\mathbf{v}}$  and  $\tilde{p}$  which are defined in the entire domain  $\Omega$ , actually represent  $\mathbf{v}|_{\Omega_s^t}$ ,  $p|_{\Omega_s^t}$ ,  $\tilde{\mathbf{v}}|_{\Omega_s^t}$  and  $\tilde{p}|_{\Omega_s^t}$  once they are involved in the inner products of structural terms defined in  $\Omega_s^t$ . Note that (16) is described in the Eulerian-updated Lagrangian frame since the entire domain  $\Omega$  is stationary thus the Eulerian description is used therein to define the real and fictitious fluid equations, whereas the updated Lagrangian description is applied to the structural domain  $\Omega_s^t$  that is kept being updated via its position variable  $\mathbf{X}_s(\hat{\mathbf{x}}, t)$  along the time  $t \in (0, T]$  determined by

$$\begin{aligned}\frac{\partial \mathbf{X}_s}{\partial t}(\hat{\mathbf{x}}, t) &= \mathbf{v}(\mathbf{X}_s(\hat{\mathbf{x}}, t), t), \quad \text{in } \Omega_s^0 \times [0, T], \\ \mathbf{X}_s(\hat{\mathbf{x}}, 0) &= \mathbf{X}_s^0, \quad \text{in } \Omega_s^0.\end{aligned}\quad (18)$$

### 3.2. Derivation of an IBM-based strong form

If we transfer all terms associated with  $\Omega_s^t$  in (16) back to the initial domain of structure,  $\Omega_s^0$ , then we have the following alternative weak formulation in Eulerian-total Lagrangian description,

$$\begin{aligned} & \left( \rho_f \frac{D\mathbf{v}}{Dt}, \tilde{\mathbf{v}} \right)_{\Omega} + 2(\mu_f \mathbf{D}(\mathbf{v}), \mathbf{D}(\tilde{\mathbf{v}}))_{\Omega} - (p, \nabla \cdot \tilde{\mathbf{v}})_{\Omega} + \left( (\rho_s - \rho_f) J \frac{\partial^2 \mathbf{X}_s}{\partial t^2}, \tilde{\mathbf{v}}(\mathbf{X}_s(\hat{\mathbf{x}}, t)) \right)_{\Omega_s^0} \\ & + (\mu_s J(\mathbf{F} - \mathbf{F}^{-T}), \nabla_{\hat{\mathbf{x}}} \tilde{\mathbf{v}}(\mathbf{X}_s(\hat{\mathbf{x}}, t)))_{\Omega_s^0} - 2(\mu_f J[\nabla_{\hat{\mathbf{x}}} \mathbf{v}(\mathbf{X}_s(\hat{\mathbf{x}}, t)) \mathbf{F}^{-1} + \mathbf{F}^{-T} \nabla_{\hat{\mathbf{x}}} \mathbf{v}(\mathbf{X}_s(\hat{\mathbf{x}}, t))^T], \nabla_{\hat{\mathbf{x}}} \tilde{\mathbf{v}}(\mathbf{X}_s(\hat{\mathbf{x}}, t)))_{\Omega_s^0} \\ & = (\rho_f \mathbf{g}, \tilde{\mathbf{v}})_{\Omega} + ((\rho_s - \rho_f) J \mathbf{g}, \tilde{\mathbf{v}}(\mathbf{X}_s(\hat{\mathbf{x}}, t)))_{\Omega_s^0} + \langle \mathbf{f}_{f,N}, \tilde{\mathbf{v}} \rangle_{\partial \Omega_{f,N}^t} - \langle J f_{s,CW}(\mathbf{X}_s(\hat{\mathbf{x}}, t)), \tilde{\mathbf{v}}(\mathbf{X}_s(\hat{\mathbf{x}}, t)) \cdot \hat{\mathbf{n}} \rangle_{\Gamma_C^0}, \quad (19) \\ & (\nabla \cdot \mathbf{v}, \tilde{p})_{\Omega} = 0, \quad \forall (\tilde{\mathbf{v}}, \tilde{p}) \in \mathbf{V}_0 \times W, \quad (20) \end{aligned}$$

where the structure domain remains as the initial one,  $\Omega_s^0$ , and the one-to-one Lagrangian mapping,  $\mathbf{X}_s(t) : \Omega_s^0 \rightarrow \Omega_s^t$ , is used to update the current position of the structure,  $\mathbf{x} \in \Omega_s^t$ , as  $\mathbf{x} = \mathbf{X}_s(\hat{\mathbf{x}}, t) = \hat{\mathbf{x}} + \hat{\mathbf{u}}_s$  for any  $\hat{\mathbf{x}} \in \Omega_s^0$ . Thus the total Lagrangian description is used in  $\Omega_s^0$  while the entire domain  $\Omega$  remains Eulerian.

Applying the defining property of the  $d$ -dimensional Dirac delta distribution to any  $\tilde{\mathbf{v}} \in \mathbf{V}_0$  as follows,

$$\tilde{\mathbf{v}}(\mathbf{X}_s(\hat{\mathbf{x}}, t)) = \int_{\Omega} \tilde{\mathbf{v}}(\mathbf{x}) \delta(\mathbf{x} - \mathbf{X}_s(\hat{\mathbf{x}}, t)) d\mathbf{x}, \quad \forall \hat{\mathbf{x}} \in \Omega_s^0, \quad (21)$$

we can reformulate, for example, the fourth term on the left hand side of (19) as follows,

$$\begin{aligned} \left( (\rho_s - \rho_f) J \frac{\partial^2 \mathbf{X}_s}{\partial t^2}, \tilde{\mathbf{v}}(\mathbf{X}_s(\hat{\mathbf{x}}, t)) \right)_{\Omega_s^0} &= \int_{\Omega_s^0} (\rho_s - \rho_f) J \frac{\partial^2 \mathbf{X}_s}{\partial t^2}(\hat{\mathbf{x}}, t) \left( \int_{\Omega} \tilde{\mathbf{v}}(\mathbf{x}) \delta(\mathbf{x} - \mathbf{X}_s(\hat{\mathbf{x}}, t)) d\mathbf{x} \right) d\hat{\mathbf{x}} \\ &= \int_{\Omega} \left( \int_{\Omega_s^0} (\rho_s - \rho_f) J \frac{\partial^2 \mathbf{X}_s}{\partial t^2}(\hat{\mathbf{x}}, t) \delta(\mathbf{x} - \mathbf{X}_s(\hat{\mathbf{x}}, t)) d\hat{\mathbf{x}} \right) \tilde{\mathbf{v}}(\mathbf{x}) d\mathbf{x} \\ &= \left( \int_{\Omega_s^0} (\rho_s - \rho_f) J \frac{\partial^2 \mathbf{X}_s}{\partial t^2} \delta(\mathbf{x} - \mathbf{X}_s(\hat{\mathbf{x}}, t)) d\hat{\mathbf{x}}, \tilde{\mathbf{v}} \right)_{\Omega}, \quad (22) \end{aligned}$$

or, reformulate the more complicated fifth term on the left hand side of (19) by integrating by parts first then using (21) as follows,

$$\begin{aligned} (\mu_s J(\mathbf{F} - \mathbf{F}^{-T}), \nabla_{\hat{\mathbf{x}}} \tilde{\mathbf{v}}(\mathbf{X}_s(\hat{\mathbf{x}}, t)))_{\Omega_s^0} &= - \int_{\Omega_s^0} \nabla_{\hat{\mathbf{x}}} \cdot (\mu_s J(\mathbf{F} - \mathbf{F}^{-T})) \left( \int_{\Omega} \tilde{\mathbf{v}}(\mathbf{x}) \delta(\mathbf{x} - \mathbf{X}_s(\hat{\mathbf{x}}, t)) d\mathbf{x} \right) d\hat{\mathbf{x}} \\ &+ \int_{\partial \Omega_s^0} (\mu_s J(\mathbf{F} - \mathbf{F}^{-T})) \hat{\mathbf{n}} \cdot \left( \int_{\Omega} \tilde{\mathbf{v}}(\mathbf{x}) \delta(\mathbf{x} - \mathbf{X}_s(\hat{\mathbf{x}}, t)) d\mathbf{x} \right) d\hat{s} \\ &= - \left( \int_{\Omega_s^0} \nabla_{\hat{\mathbf{x}}} \cdot (\mu_s J(\mathbf{F} - \mathbf{F}^{-T})) \delta(\mathbf{x} - \mathbf{X}_s(\hat{\mathbf{x}}, t)) d\hat{\mathbf{x}}, \tilde{\mathbf{v}} \right)_{\Omega} \\ &+ \left( \int_{\partial \Omega_s^0} (\mu_s J(\mathbf{F} - \mathbf{F}^{-T})) \hat{\mathbf{n}} \delta(\mathbf{x} - \mathbf{X}_s(\hat{\mathbf{x}}, t)) d\hat{s}, \tilde{\mathbf{v}} \right)_{\Omega}. \quad (23) \end{aligned}$$

Similarly, we can also reformulate the rest structural terms in (19). Then, conducting the integration by parts as well for the second term on the left hand side of (19), and considering that  $\tilde{\mathbf{v}}$  is arbitrary in  $\mathbf{V}_0$ , we can obtain the following

strong form of the dimensional momentum equation,

$$\begin{aligned}
& \rho_f \frac{D\mathbf{v}}{Dt} - \nabla \cdot (2\mu_f \mathbf{D}(\mathbf{v})) + \nabla p + \int_{\Omega_s^0} (\rho_s - \rho_f) J \frac{\partial^2 \mathbf{X}_s}{\partial t^2} \delta(\mathbf{x} - \mathbf{X}_s(\hat{\mathbf{x}}, t)) d\hat{\mathbf{x}} \\
& - \int_{\Omega_s^0} \nabla_{\hat{\mathbf{x}}} \cdot (\mu_s J (\mathbf{F} - \mathbf{F}^{-T})) \delta(\mathbf{x} - \mathbf{X}_s(\hat{\mathbf{x}}, t)) d\hat{\mathbf{x}} + \int_{\partial\Omega_s^0} (\mu_s J (\mathbf{F} - \mathbf{F}^{-T})) \hat{\mathbf{n}} \delta(\mathbf{x} - \mathbf{X}_s(\hat{\mathbf{x}}, t)) d\hat{s} \\
& + \int_{\Omega_s^0} \nabla_{\hat{\mathbf{x}}} \cdot (\mu_f J [\nabla_{\hat{\mathbf{x}}} \mathbf{v}(\mathbf{X}_s(\hat{\mathbf{x}}, t)) \mathbf{F}^{-1} + \mathbf{F}^{-T} \nabla_{\hat{\mathbf{x}}} \mathbf{v}(\mathbf{X}_s(\hat{\mathbf{x}}, t))^T]) \delta(\mathbf{x} - \mathbf{X}_s(\hat{\mathbf{x}}, t)) d\hat{\mathbf{x}} \\
& - \int_{\partial\Omega_s^0} (\mu_f J [\nabla_{\hat{\mathbf{x}}} \mathbf{v}(\mathbf{X}_s(\hat{\mathbf{x}}, t)) \mathbf{F}^{-1} + \mathbf{F}^{-T} \nabla_{\hat{\mathbf{x}}} \mathbf{v}(\mathbf{X}_s(\hat{\mathbf{x}}, t))^T]) \hat{\mathbf{n}} \delta(\mathbf{x} - \mathbf{X}_s(\hat{\mathbf{x}}, t)) d\hat{s} \\
& = \rho_f \mathbf{g} + \int_{\Omega_s^0} (\rho_s - \rho_f) J \mathbf{g} \delta(\mathbf{x} - \mathbf{X}_s(\hat{\mathbf{x}}, t)) d\hat{\mathbf{x}} - \int_{\Gamma_s^0} J f_{s,C_W}(\mathbf{X}_s(\hat{\mathbf{x}}, t)) \delta(\mathbf{x} - \mathbf{X}_s(\hat{\mathbf{x}}, t)) d\hat{s}, \quad \text{in } \Omega \times (0, T], \quad (24)
\end{aligned}$$

and the strong form of the dimensional mass equation due to the arbitrary  $\tilde{p} \in W$ ,

$$\nabla \cdot \mathbf{v} = 0, \quad \text{in } \Omega \times (0, T], \quad (25)$$

where  $\mathbf{F} = \nabla_{\hat{\mathbf{x}}} \mathbf{X}_s(\hat{\mathbf{x}}, t) = \nabla_{\hat{\mathbf{x}}} \mathbf{x}(\hat{\mathbf{x}}, t)$ , and  $\mathbf{X}_s(\hat{\mathbf{x}}, t)$  satisfies (18). The strong form (24) and (25) subject to the following boundary and initial conditions,

$$\begin{aligned}
\mathbf{v} &= \begin{cases} \mathbf{v}_{f,D}, & \text{on } \partial\Omega_{f,D}^t \times [0, T], \\ \mathbf{v}_{s,D}, & \text{on } \partial\Omega_s^t \setminus \Gamma^t \times [0, T], \end{cases} \\
(-p\mathbf{I} + 2\mu_f \mathbf{D}(\mathbf{v})) \mathbf{n}_{f,N} &= \mathbf{f}_{f,N}, \quad \text{on } \partial\Omega_{f,N}^t \times [0, T], \\
\mathbf{v}(\mathbf{x}, 0) &= \begin{cases} \mathbf{v}_f^0, & \text{in } \Omega_f, \\ \mathbf{v}_s^0, & \text{in } \Omega_s. \end{cases} \quad (26)
\end{aligned}$$

The above derivations are completely reversible, i.e., we can trace all the way back to regain (19) and (20), which means (19) and (20), or further back, (16) and (17) are also the weak formulation of the strong forms (24)-(26). In fact, (24)-(26) generally demonstrate the mathematical modeling of FSCI based on IBM. It is well known that the original IBM [44, 45] was carried out by means of the finite difference scheme to approximate the strong form that involves the Dirac delta function everywhere, such as (24)-(26) here that requires the construction of suitable approximations to the Dirac delta distribution in order to discretize the terms in (24) that contains the Dirac delta function. Our goal in this paper is to propose a continuous Galerkin (CG) finite element approximation to the fluidic and structure equations, as well as to the Lagrangian mapping  $\mathbf{X}_s$  that describes the position of immersed structure along the time, within the frame of unified-field monolithic fictitious domain method without introducing the Dirac delta function, the Jacobian matrix  $\mathbf{F}$  and the Jacobian  $J$  into the structural terms. To that end, we will develop our fictitious domain-finite element approximation based on (16) and (17) in the next section, thus there is no need to discretize the Dirac delta function and no need to deal with the complicated nonlinear coefficients that involve  $\mathbf{F}$  and  $J$  in the structural terms. All of these can be considered as significant improvements over the original IBM.

#### 4. Unified-field monolithic fictitious domain-finite element method

In this section, we describe how the unified-field, monolithic fictitious domain-finite element method (UFMFD-FEM) is developed on the basis of the weak formulation (16) and (17). First of all, we introduce a fixed Eulerian mesh,  $\mathcal{T}_h = \bigcup_{k=1}^M e_k$  ( $0 < h < 1$ ), to triangulate the entire (real and fictitious) fluid domain  $\Omega$  for up to  $M$  simplicial fluid elements  $e_k$  ( $1 \leq k \leq M$ ), and adopt an updated Lagrangian mesh,  $\mathcal{T}_{h_s}^t = \bigcup_{k=1}^{M_s} e_{s,k}^t$  ( $0 < h_s < 1$ ), to triangulate the structural domain  $\Omega_s^t$  along the time  $t \in [0, T]$  for up to  $M_s$  simplicial structural elements  $e_{s,k}^t$  ( $1 \leq k \leq M_s$ ) and

$N_s$  structural nodes, where  $h_s$  can be different from  $h$ , and,  $\mathcal{T}_h$  and  $\mathcal{T}_{h_s}^t$  are nonconforming through the interface  $\Gamma^t$  for all  $t \in [0, T]$ , as illustrated in the right of Figure 1. Therefore, material derivatives in these two different domains have different expressions, as introduced before and restated below,

$$\frac{D\mathbf{v}}{Dt} = \begin{cases} \frac{\partial \mathbf{v}}{\partial t} + \mathbf{v} \cdot \nabla \mathbf{v}, & \text{in } \Omega \times [0, T], \\ \frac{\partial \mathbf{v}}{\partial t} = \frac{\partial^2 \mathbf{X}_s}{\partial t^2} \circ \mathbf{X}_s^{-1}, & \text{in } \Omega_s^t \times [0, T]. \end{cases} \quad (27)$$

To discretize the temporal derivatives in (27), we introduce a uniform partition  $0 = t_0 < t_1 < \dots < t_N = T$  with the time-step size  $\Delta t = T/N$ , and set  $t^n = n\Delta t$ ,  $\varphi^n = \varphi(\mathbf{x}, t^n)$  for  $n = 1, \dots, N$ .

#### 4.1. Reformulation of the deviatoric stress in update Lagrangian frame

Since we now adopt the updated Lagrangian frame to describe the structure motion, we shall update the deviatoric stress term of the structure in (16) at the current  $(n+1)$ -th time step, i.e.,  $\boldsymbol{\tau}_s^{n+1} := \mu_s(\mathbf{F}^{n+1}(\mathbf{F}^{n+1})^T - \mathbf{I})$ , by utilizing the spatial gradient  $\nabla_{\mathbf{x}^n} \mathbf{x}^{n+1}$  that is computed on the known coordinate at the previous  $n$ -th time step,  $\mathbf{x}^n = \mathbf{X}_s(\hat{\mathbf{x}}, t^n) = \mathbf{X}_s^n \in \Omega_s^n$ , instead of using  $\nabla_{\hat{\mathbf{x}}} \mathbf{x}^{n+1}$  to directly compute  $\mathbf{F}^{n+1}$  which however belongs to the total Lagrangian description. To do so, we employ the chain rule to reformulate  $\boldsymbol{\tau}_s^{n+1}$  through  $\mathbf{x}^n$ , leading to

$$\begin{aligned} \boldsymbol{\tau}_s^{n+1} &= \mu_s (\nabla_{\hat{\mathbf{x}}} \mathbf{x}^{n+1} (\nabla_{\hat{\mathbf{x}}} \mathbf{x}^{n+1})^T - \mathbf{I}) \\ &= \mu_s (\nabla_{\mathbf{x}^n} \mathbf{x}^{n+1} (\nabla_{\mathbf{x}^n} \mathbf{x}^{n+1})^T - \mathbf{I}) + \mu_s \nabla_{\mathbf{x}^n} \mathbf{x}^{n+1} (\nabla_{\hat{\mathbf{x}}} \mathbf{x}^n (\nabla_{\hat{\mathbf{x}}} \mathbf{x}^n)^T - \mathbf{I}) (\nabla_{\mathbf{x}^n} \mathbf{x}^{n+1})^T \\ &= \mu_s (\nabla_{\mathbf{x}^n} \mathbf{x}^{n+1} (\nabla_{\mathbf{x}^n} \mathbf{x}^{n+1})^T - \mathbf{I}) + \nabla_{\mathbf{x}^n} \mathbf{x}^{n+1} \boldsymbol{\tau}_s^n (\nabla_{\mathbf{x}^n} \mathbf{x}^{n+1})^T, \end{aligned} \quad (28)$$

where  $\boldsymbol{\tau}_s^n$  is defined in  $\Omega_s^n$  in the sense that  $\boldsymbol{\tau}_s^n = \boldsymbol{\tau}_s(\mathbf{x}^n, t^n)$ . It is easy to see  $\boldsymbol{\tau}_s^0 = \mathbf{0}$ .

Integrate (18) in time from  $t^n$  to  $t^{n+1}$ , yields

$$\mathbf{X}_s^{n+1} = \mathbf{X}_s^n + \int_{t^n}^{t^{n+1}} \mathbf{v}(\mathbf{X}_s(\hat{\mathbf{x}}, t), t) dt, \quad \text{or,} \quad \mathbf{x}^{n+1} = \mathbf{x}^n + \int_{t^n}^{t^{n+1}} \mathbf{v}(\mathbf{x}(\hat{\mathbf{x}}, t), t) dt. \quad (29)$$

Applying (29) to (28), we can further reformulate  $\boldsymbol{\tau}_s^{n+1}$  as follows,

$$\begin{aligned} \boldsymbol{\tau}_s^{n+1} &= \mu_s \left( \left( \mathbf{I} + \int_{t^n}^{t^{n+1}} \nabla_{\mathbf{x}^n} \mathbf{v} dt \right) \left( \mathbf{I} + \int_{t^n}^{t^{n+1}} \nabla_{\mathbf{x}^n} \mathbf{v} dt \right)^T - \mathbf{I} \right) + \left( \mathbf{I} + \int_{t^n}^{t^{n+1}} \nabla_{\mathbf{x}^n} \mathbf{v} dt \right) \boldsymbol{\tau}_s^n \left( \mathbf{I} + \int_{t^n}^{t^{n+1}} \nabla_{\mathbf{x}^n} \mathbf{v} dt \right)^T \\ &= \mu_s \left( \int_{t^n}^{t^{n+1}} \nabla_{\mathbf{x}^n} \mathbf{v} dt + \left( \int_{t^n}^{t^{n+1}} \nabla_{\mathbf{x}^n} \mathbf{v} dt \right)^T + \int_{t^n}^{t^{n+1}} \nabla_{\mathbf{x}^n} \mathbf{v} dt \left( \int_{t^n}^{t^{n+1}} \nabla_{\mathbf{x}^n} \mathbf{v} dt \right)^T \right) + \boldsymbol{\tau}_s^n + \\ &\quad \int_{t^n}^{t^{n+1}} \nabla_{\mathbf{x}^n} \mathbf{v} dt \boldsymbol{\tau}_s^n + \boldsymbol{\tau}_s^n \left( \int_{t^n}^{t^{n+1}} \nabla_{\mathbf{x}^n} \mathbf{v} dt \right)^T + \int_{t^n}^{t^{n+1}} \nabla_{\mathbf{x}^n} \mathbf{v} dt \boldsymbol{\tau}_s^n \left( \int_{t^n}^{t^{n+1}} \nabla_{\mathbf{x}^n} \mathbf{v} dt \right)^T. \end{aligned} \quad (30)$$

Utilizing a proper quadrature rule to discretize the temporal integrals in (30), e.g., simply picking up the right-endpoint rule, we can obtain

$$\boldsymbol{\tau}_s^{n+1} = \mu_s \Delta t (\nabla_{\mathbf{x}^n} \mathbf{v}^{n+1} + (\nabla_{\mathbf{x}^n} \mathbf{v}^{n+1})^T + \Delta t \nabla_{\mathbf{x}^n} \mathbf{v}^{n+1} (\nabla_{\mathbf{x}^n} \mathbf{v}^{n+1})^T) + \boldsymbol{\tau}_s^n + \Delta t \nabla_{\mathbf{x}^n} \mathbf{v}^{n+1} \boldsymbol{\tau}_s^n + \Delta t \boldsymbol{\tau}_s^n (\nabla_{\mathbf{x}^n} \mathbf{v}^{n+1})^T + (\Delta t)^2 \nabla_{\mathbf{x}^n} \mathbf{v}^{n+1} \boldsymbol{\tau}_s^n (\nabla_{\mathbf{x}^n} \mathbf{v}^{n+1})^T + O((\Delta t)^2). \quad (31)$$

#### 4.2. Full discretization of the UFMFD-FEM

First, we introduce the following finite element spaces in which the velocity and pressure are discretized, respectively,

$$\begin{aligned} \mathbf{V}_h &:= \{ \tilde{\mathbf{v}} \in \mathbf{V} \mid \tilde{\mathbf{v}}|_{e_k} \in P_m(e_k)^d, \forall e_k \in \mathcal{T}_h \}, & \mathbf{V}_{0,h} &:= \{ \tilde{\mathbf{v}} \in \mathbf{V}_0 \mid \tilde{\mathbf{v}}|_{e_k} \in P_m(e_k)^d, \forall e_k \in \mathcal{T}_h \}, \\ W_h &:= \{ \tilde{p} \in W \mid \tilde{p}|_{e_k} \in P_1(e_k), \forall e_k \in \mathcal{T}_h \}, \end{aligned} \quad (32)$$

where  $P_k$  denotes the  $k$ -th degree piecewise polynomial space. Here we can either employ the Taylor-Hood  $(P_2/P_1)$  mixed finite element by letting  $m = 2$  in (32), or the lowest equal-order mixed  $P_1/P_1$  element by letting  $m = 1$  in (32)

with the pressure stabilization scheme [23, 54, 7, 33, 37], to approximate the saddle-point problem arising from the weak form (16) and (17) in the finite element spaces  $\mathbf{V}_h \times W_h \subset \mathbf{V} \times W$ . The different choice of  $m$  in (32) will lead to a large difference on the computational cost due to the quadratic element involved in  $P_2/P_1$  mixed element with at least twice as many degrees of freedom (DOFs) of the velocity variable as the linear element in  $P_1/P_1$  mixed element. On the other hand, the  $P_1/P_1$  element with pressure stabilization needs an empirically well tuned stabilization parameter to make its approximation stable and accurate. Their use on real world problems sometimes depends on the practical interest. In fact, with a reasonably acceptable accuracy, if the computational efficiency is more preferred in practice, then the  $P_1/P_1$  element with pressure stabilization scheme is superior to the  $P_2/P_1$  element.

Moreover, we choose the backward Euler scheme to approximate temporal derivatives in (27), resulting in the following fully discrete UFMFD-FEM for the FSI model presented in Section 2. We first interpolate the initial value function  $\mathbf{v}(\mathbf{x}, 0)$ , which is defined in (26), into  $\mathbf{V}_h$  to get the discrete initial value  $\mathbf{v}_h^0 = \prod_h \mathbf{v}(\mathbf{x}, 0) \in \mathbf{V}_h$ , where the interpolation operator,  $\prod_h$ , is described by the definition of  $\mathbf{V}_h$  in (32). Then, we define the following fully discrete UFMFD-FEM: for  $n = 0, 1, \dots, N-1$  and  $\forall(\tilde{\mathbf{v}}_h, \tilde{p}_h) \in \mathbf{V}_{0,h} \times W_h$ , find  $(\mathbf{v}_h^{n+1}, p_h^{n+1}) \in \mathbf{V}_h \times W_h$  such that

$$\begin{aligned} & \left( \rho_f \frac{\mathbf{v}_h^{n+1} - \mathbf{v}_h^n}{\Delta t}, \tilde{\mathbf{v}}_h \right)_\Omega + (\rho_f \mathbf{v}_h^{n+1} \cdot \nabla \mathbf{v}_h^{n+1}, \tilde{\mathbf{v}}_h)_\Omega + 2(\mu_f \mathbf{D}(\mathbf{v}_h^{n+1}), \mathbf{D}(\tilde{\mathbf{v}}_h))_\Omega - (p_h^{n+1}, \nabla \cdot \tilde{\mathbf{v}}_h)_\Omega - (\nabla \cdot \mathbf{v}_h^{n+1}, \tilde{p}_h)_\Omega \\ & + \left( (\rho_s - \rho_f) \frac{\mathbf{v}_h^{n+1}|_{\Omega_s^n} - \mathbf{v}_h^n|_{\Omega_s^n}}{\Delta t}, \tilde{\mathbf{v}}_h|_{\Omega_s^n} \right)_{\Omega_s^n} + \left( \boldsymbol{\tau}_{s,h}^{n+1}, \nabla_{\mathbf{x}^n} \tilde{\mathbf{v}}_h|_{\Omega_s^n} \right)_{\Omega_s^n} - 2 \left( \mu_f \mathbf{D}(\mathbf{v}_h^{n+1}|_{\Omega_s^n}), \mathbf{D}(\tilde{\mathbf{v}}_h|_{\Omega_s^n}) \right)_{\Omega_s^n} \\ & - \sum_{k=1}^M \xi_k (\mathbf{R}_h^{n+1}, \nabla \tilde{p}_h)_{e_k} = (\rho_f \mathbf{g}, \tilde{\mathbf{v}}_h)_\Omega + \left( (\rho_s - \rho_f) \mathbf{g}, \tilde{\mathbf{v}}_h|_{\Omega_s^n} \right)_{\Omega_s^n} + \langle \mathbf{f}_{f,N}^{n+1}, \tilde{\mathbf{v}}_h \rangle_{\partial \Omega_{f,N}^n} - \langle \mathbf{f}_{s,CW}^{n+1}, \tilde{\mathbf{v}}_h|_{\Gamma_C^n} \cdot \mathbf{n} \rangle_{\Gamma_C^n}, \end{aligned} \quad (33)$$

where the discrete deviatoric stress  $\boldsymbol{\tau}_{s,h}^{n+1}$ , which approximates to  $\boldsymbol{\tau}_s^{n+1}$  defined in (31), is defined as

$$\begin{aligned} \boldsymbol{\tau}_{s,h}^{n+1} &= \mu_s \Delta t \left( \nabla_{\mathbf{x}^n} \mathbf{v}_h^{n+1}|_{\Omega_s^n} + \left( \nabla_{\mathbf{x}^n} \mathbf{v}_h^{n+1}|_{\Omega_s^n} \right)^T + \Delta t \nabla_{\mathbf{x}^n} \mathbf{v}_h^{n+1}|_{\Omega_s^n} \left( \nabla_{\mathbf{x}^n} \mathbf{v}_h^{n+1}|_{\Omega_s^n} \right)^T \right) + \boldsymbol{\tau}_{s,h}^n + \\ & \Delta t \nabla_{\mathbf{x}^n} \mathbf{v}_h^{n+1}|_{\Omega_s^n} \boldsymbol{\tau}_{s,h}^n + \Delta t \boldsymbol{\tau}_{s,h}^n \left( \nabla_{\mathbf{x}^n} \mathbf{v}_h^{n+1}|_{\Omega_s^n} \right)^T + (\Delta t)^2 \nabla_{\mathbf{x}^n} \mathbf{v}_h^{n+1}|_{\Omega_s^n} \boldsymbol{\tau}_{s,h}^n \left( \nabla_{\mathbf{x}^n} \mathbf{v}_h^{n+1}|_{\Omega_s^n} \right)^T. \end{aligned} \quad (34)$$

Note that in (33) all structural integrals are processed in the known structural domain at the  $n$ -th time step,  $\Omega_s^n$ , which is essential, thus the discrete deviatoric stress,  $\boldsymbol{\tau}_{s,h}^{n+1}$ , is defined in  $\Omega_s^n$  that makes an accurate sense because all involved spatial gradients in (34) are for the restriction of  $\mathbf{v}_h^{n+1}$  in  $\Omega_s^n$  with respect to  $\mathbf{x}^n \in \Omega_s^n$ , and, the involved  $\boldsymbol{\tau}_{s,h}^n$  belongs to  $\Omega_s^n$  as well in the sense that  $\boldsymbol{\tau}_{s,h}^n = \boldsymbol{\tau}_{s,h}(\mathbf{x}^n, t^n)$ . We will discuss in Section 4.3 about how to compute  $\boldsymbol{\tau}_{s,h}^n$  by means of the finite element discretization in  $\Omega_s^n$ , for  $n = 0, 1, \dots, N-1$ .

If  $m = 2$  is chosen in (32), then the last term on the left hand side of (33) vanishes, otherwise it remains with  $m = 1$  as the pressure stabilization term defined in all (real and fictitious) fluidic elements,  $e_k \in \mathcal{T}_h$  ( $k = 1, \dots, M$ ), elementwisely, where  $\mathbf{R}_h^{n+1}$  is the discrete residual of the momentum equation of both the real and fictitious fluid at the  $(n+1)$ -th time step, which is defined below in terms of the unified finite element solution  $(\mathbf{v}_h, p_h)$  that is only associated with  $\mathcal{T}_h$ ,

$$\mathbf{R}_h^{n+1} = \rho_f \frac{\mathbf{v}_h^{n+1} - \mathbf{v}_h^n}{\Delta t} + \rho_f \mathbf{v}_h^{n+1} \cdot \nabla \mathbf{v}_h^{n+1} + \nabla p_h^{n+1} - \rho_f \mathbf{g}, \quad (35)$$

in which the viscous term (the second-order spatial derivative term) vanishes from  $\mathbf{R}_h^{n+1}$  since  $\mathbf{v}_h \in \mathbf{V}_h$  that is discretized by piecewise linear ( $P_1$ ) polynomials.  $\xi_k$  ( $1 \leq k \leq M$ ) is the pressure stabilization parameter that may affect the computational results dearly. According to the usual choices of the pressure stabilization parameter

[37, 54, 12, 40], we define the following elementwise stabilization parameter  $\xi_k$ ,

$$\xi_k = \left[ \left( \zeta_0 \frac{\rho_f}{\Delta t} \right)^2 + \left( \zeta_1 \frac{\mu_f}{h_k^2} \right)^2 + \left( \zeta_2 \frac{\rho_f \|\mathbf{v}_h^{n+1}\|}{h_k} \right)^2 \right]^{-\frac{1}{2}}, \quad (36)$$

where  $\zeta_i$  ( $i = 0, 1, 2$ ) are the tunable, dimensionless parameters that are independent of the element length,  $h_k$  ( $1 \leq k \leq M$ ), and, their exact values can only be determined empirically.

In addition, since both the trial function  $\mathbf{v}_h \in \mathbf{V}_h$  and the test function  $\tilde{\mathbf{v}}_h \in \mathbf{V}_{0,h}$  in (33) are associated with the fixed Eulerian mesh  $\mathcal{T}_h$  only, to compute all structural terms in (33), we need to interpolate both  $\mathbf{v}_h$  and  $\tilde{\mathbf{v}}_h$  into the updated Lagrangian mesh  $\mathcal{T}_{h_s}^n$  in  $\Omega_s^n$ , which are represented by  $\phi_h|_{\Omega_s^n}$  in (33) and (34), generally. A detailed interpolation procedure for how to implement  $\phi_h|_{\Omega_s^n}$  from  $\mathcal{T}_h$  to  $\mathcal{T}_{h_s}^n$  is described in Appendix A.

**Remark 4.1.** *Although a rigorous error analysis for the proposed UFMFD-FEM (33)-(36) is not yet studied in this paper (which will be considered in our next work), we suppose that the proposed method may own a similar convergence property with that of the distributed Lagrange multiplier/fictitious domain (DLM/FD)-finite element method for various interface problems [5, 55, 35, 50, 51], i.e., when  $h_s/h \approx 1$ , the spatial convergence rate of our developed UFMFD-FEM with a pressure-stabilized  $P_1/P_1$  mixed element for the velocity and pressure on a quasi-uniform grid supposes to be*

$$\|\mathbf{v} - \mathbf{v}_h\|_{L^2(\Omega)^d} = O(h^r), \quad \|p - p_h\|_{L^2(\Omega)} = O(h^q), \quad \text{for } \mathbf{v} \in H^r(\Omega)^d \quad (1 < r \leq 3/2) \text{ and } p \in H^q(\Omega) \quad (0 < q \leq 1/2), \quad (37)$$

while its temporal convergence rate is of the first order, i.e.,  $O(\Delta t)$  due to the employment of backward Euler scheme on the temporal discretization. We will attempt to prove (37) in our next paper based upon the Babuška–Brezzi’s theory [4, 8] by proving a corresponding inf-sup condition of a properly defined total bilinear form associated with the saddle-point problem that is involved in the developed UFMFD-FEM, as we do in [55, 35, 50, 51]. In this paper, we focus more on the development of advanced numerical discretizations and algorithms, as well as their numerical validations through benchmark problems, therefore instead of proving (37) theoretically, we conduct a series of numerical convergence tests to validate (37), as shown in Section 6.

#### 4.3. Post-processing the structural information

After obtaining  $\mathbf{v}_h^{n+1}$  from (33), we then use,

$$\mathbf{X}_{s,h_s}^{n+1} = \mathbf{X}_{s,h_s}^n + \Delta t \mathbf{v}_h^{n+1}|_{\Omega_s^n}, \quad (38)$$

at the  $(n+1)$ -th time step to attain the position of the immersed structure domain,  $\Omega_s^{n+1}$ , or, the updated Lagrangian mesh of the structure,  $\mathcal{T}_{h_s}^{n+1}$ , for  $n = 0, 1, \dots, N-1$ , where  $\mathbf{X}_{s,h_s}^0$  denotes the initial structural position that is also discretized by  $\mathcal{T}_{h_s}^0$ , on which we set  $\boldsymbol{\tau}_{s,h}^0 = \mathbf{0}$ .

Instead of a direct interpolation, we can employ the  $L^2$ -projection method to compute  $\mathbf{v}_h^{n+1}|_{\Omega_s^n}$  shown in (38) within the structure domain  $\Omega_s^n$  in a more accurate fashion. To do so, we first define the following finite element spaces in  $\Omega_s^t \times [0, T]$ ,

$$\begin{aligned} \mathbf{U}_{h_s}^0 &:= \{ \phi \in L^2(\Omega_s^0)^d \mid \phi|_{e_{s,k}^0} \in P_1(e_{s,k}^0)^d, \forall e_{s,k}^0 \in \mathcal{T}_{h_s}^0 \}, \\ \mathbf{U}_{h_s}^t &:= \{ \phi : \Omega_s^t \times [0, T] \rightarrow \mathbb{R}^d \mid \phi = \hat{\phi} \circ \mathbf{X}_{s,h_s}^{-1}(t), \forall \hat{\phi} \in \mathbf{U}_{h_s}^0 \}, \end{aligned} \quad (39)$$

where  $\mathbf{X}_{s,h_s}(t) : \Omega_s^0 \rightarrow \Omega_s^t$  is a discrete Lagrangian mapping approximated by  $P_1^d$  Lagrange-type finite elements such that  $\mathbf{x}(\hat{\mathbf{x}}, t) = \mathbf{X}_{s,h_s}(\hat{\mathbf{x}}, t)$  for any  $\mathbf{x} \in \mathcal{T}_{h_s}^t$  that corresponds to its initial position  $\hat{\mathbf{x}} \in \mathcal{T}_{h_s}^0$ . And, due to the following long-standing Proposition 4.2 (see, e.g., [16]), we know  $\mathbf{U}_{h_s}^t \subset L^2(\Omega_s^t)^d$ .

**Proposition 4.2.** *Consider  $\Omega_1$  and  $\Omega_2$  are two bounded open subsets of  $\mathbb{R}^d$ , and assume  $\mathbf{X} \in W^{1,\infty}(\Omega_1)$ . Suppose also that  $\mathbf{X} : \Omega_1 \rightarrow \Omega_2$  is invertible and such that  $\mathbf{X}^{-1} \in W^{1,\infty}(\Omega_2)$ . Then for any  $u \in H^1(\Omega_2)$  we have  $u \circ \mathbf{X} \in H^1(\Omega_1)$ .*

Now we can define the following  $L^2$ -projection for  $\mathbf{v}_h^{n+1}|_{\Omega_s^n}$  by the finite element discretization: find  $\phi_{h_s}^n \in \mathbf{U}_{h_s}^n$  such that

$$\left(\phi_{h_s}^n, \tilde{\phi}\right)_{\Omega_s^n} = \sum_{k=1}^{M_s} \left(\mathbf{v}_h^{n+1}|_{\Omega_s^n}, \tilde{\phi}\right)_{e_{s,k}^{n+1}}, \quad \forall \tilde{\phi} \in \mathbf{U}_{h_s}^n, \quad n = 0, 1, \dots, N-1. \quad (40)$$

Then, (38) can be changed to

$$\mathbf{X}_{s,h_s}^{n+1} = \mathbf{X}_{s,h_s}^n + \Delta t \phi_{h_s}^n, \quad n = 0, 1, \dots, N-1. \quad (41)$$

The new position of  $\Omega_s^{n+1}$  and its triangulation,  $\mathcal{T}_{h_s}^{n+1}$ , are thus updated.

Next, we can also adopt the  $L^2$  projection to update  $\boldsymbol{\tau}_{s,h}^{n+1}$  in  $\Omega_s^{n+1}$  by using the newly obtained  $\mathbf{v}_h^{n+1}$ ,  $\mathbf{X}_{s,h_s}^{n+1}$  and  $\mathcal{T}_{h_s}^{n+1}$ . Define the corresponding finite element spaces first,

$$\begin{aligned} \boldsymbol{\Upsilon}_{h_s}^0 &:= \{\phi \in L^2(\Omega_s^0)^{\frac{d(d+1)}{2}} \mid \phi|_{e_{s,k}^0} \in P_1(e_{s,k}^0)^{\frac{d(d+1)}{2}}, \forall e_{s,k}^0 \in \mathcal{T}_{h_s}^0\}, \\ \boldsymbol{\Upsilon}_{h_s}^t &:= \{\phi : \Omega_s^t \times [0, T] \rightarrow \mathbb{R}^{\frac{d(d+1)}{2}} \mid \phi = \hat{\phi} \circ \mathbf{X}_{s,h_s}^{-1}(t), \forall \hat{\phi} \in \boldsymbol{\Upsilon}_{h_s}^0\}, \end{aligned} \quad (42)$$

which leads to  $\boldsymbol{\Upsilon}_{h_s}^t \subset L^2(\Omega_s^t)^{\frac{d(d+1)}{2}}$ . On the other hand, from (31) we see  $\nabla_{\mathbf{x}^n} \mathbf{v}^{n+1}$  needs to be approximated using the obtained  $\mathbf{v}_h^{n+1}$  in the updated  $\Omega_s^{n+1}$ , i.e., we need to frequently compute its discrete version,  $\nabla_{\mathbf{x}^n} \mathbf{v}_h^{n+1}|_{\Omega_s^{n+1}}$ , in order to finally update  $\boldsymbol{\tau}_{s,h}^{n+1}$  in a discrete manner. However, it is not a direct computation because  $\mathbf{v}_h^{n+1}|_{\Omega_s^{n+1}}$ , which is defined in  $\Omega_s^{n+1}$ , takes a spatial gradient with respect to  $\mathbf{x}^n \in \Omega_s^n$ . Actually, by the chain rule we can rewrite  $\nabla_{\mathbf{x}^n} \mathbf{v}_h^{n+1}|_{\Omega_s^{n+1}} = \mathbf{G}^{n+1} \mathbf{F}^{n+1,n}$ , where  $\mathbf{G}^{n+1} := \nabla_{\mathbf{x}^{n+1}} \mathbf{v}_h^{n+1}|_{\Omega_s^{n+1}}$  that is defined in  $\Omega_s^{n+1}$ , and  $\mathbf{F}^{n+1,n} := \nabla_{\mathbf{x}^n} \mathbf{x}^{n+1}$  that can be reformulated as  $\mathbf{F}^{n+1,n} = \mathbf{I} + \Delta t \mathbf{Q}^n$ , where  $\mathbf{Q}^n := \nabla_{\mathbf{x}^n} \mathbf{v}_h^{n+1}|_{\Omega_s^n}$  due to (38). Thus  $\mathbf{F}^{n+1,n}$  is defined in  $\Omega_s^n$ , essentially. Before defining the  $L^2$ -projection for  $\boldsymbol{\tau}_{s,h}^{n+1} \in \boldsymbol{\Upsilon}_{h_s}^{n+1}$ , we first adopt the  $L^2$ -projection method to project  $\mathbf{G}^{n+1}$  onto  $\boldsymbol{\Upsilon}_{h_s}^{n+1}$ , i.e., find  $\mathbf{G}_P^{n+1} \in \boldsymbol{\Upsilon}_{h_s}^{n+1}$  such that

$$\left(\mathbf{G}_P^{n+1}, \tilde{\phi}\right)_{\Omega_s^{n+1}} = \sum_{k=1}^{M_s} \left(\mathbf{G}^{n+1}, \tilde{\phi}\right)_{e_{s,k}^{n+1}}, \quad \forall \tilde{\phi} \in \boldsymbol{\Upsilon}_{h_s}^{n+1}, \quad n = 0, 1, \dots, N-1. \quad (43)$$

Now based on (31), we are able to define the following  $L^2$ -projection for  $\boldsymbol{\tau}_{s,h}^{n+1}$  in the finite element approximation: find  $\boldsymbol{\tau}_{s,h}^{n+1} \in \boldsymbol{\Upsilon}_{h_s}^{n+1}$  such that

$$\begin{aligned} \left(\boldsymbol{\tau}_{s,h}^{n+1}, \tilde{\phi}\right)_{\Omega_s^{n+1}} &= \mu_s \Delta t \sum_{k=1}^{M_s} \left(\mathbf{G}_P^{n+1} \mathbf{F}^{n+1,n} + (\mathbf{G}_P^{n+1} \mathbf{F}^{n+1,n})^T + \Delta t \mathbf{G}_P^{n+1} \mathbf{F}^{n+1,n} (\mathbf{G}_P^{n+1} \mathbf{F}^{n+1,n})^T, \tilde{\phi}\right)_{e_{s,k}^{n+1}} \\ &+ \Delta t \sum_{k=1}^{M_s} \left(\mathbf{G}_P^{n+1} \mathbf{F}^{n+1,n} \boldsymbol{\tau}_{s,h}^n + \boldsymbol{\tau}_{s,h}^n (\mathbf{G}_P^{n+1} \mathbf{F}^{n+1,n})^T + \Delta t \mathbf{G}_P^{n+1} \mathbf{F}^{n+1,n} \boldsymbol{\tau}_{s,h}^n (\mathbf{G}_P^{n+1} \mathbf{F}^{n+1,n})^T, \tilde{\phi}\right)_{e_{s,k}^{n+1}} \\ &+ \sum_{k=1}^{M_s} \left(\boldsymbol{\tau}_{s,h}^n, \tilde{\phi}\right)_{e_{s,k}^{n+1}} = \sum_{i=1}^7 R_i, \quad \forall \tilde{\phi} \in \boldsymbol{\Upsilon}_{h_s}^{n+1}, \quad n = 0, 1, \dots, N-1, \end{aligned} \quad (44)$$

where all seven terms on the right hand side of (44), which are to be integrated in  $\Omega_s^{n+1}$ , involve integrand functions defined in  $\Omega_s^n$ , such as  $\boldsymbol{\tau}_{s,h}^n$  and  $\mathbf{Q}^n$  included in  $\mathbf{F}^{n+1,n}$  which are actually represented by a composite function with respect to  $\mathbf{x}^{n+1}$  through the discrete Lagrangian mapping  $\mathbf{X}_{s,h_s}(t)$ , i.e.,  $\boldsymbol{\tau}_{s,h}^n \circ \mathbf{X}_{s,h_s}^n (\mathbf{X}_{s,h_s}^{n+1})^{-1}(\mathbf{x}^{n+1})$  and  $\mathbf{Q}^n \circ \mathbf{X}_{s,h_s}^n (\mathbf{X}_{s,h_s}^{n+1})^{-1}(\mathbf{x}^{n+1})$ . Thus, in order to carry out all integrals on the right hand side of (44), it is necessary to change variables from  $\Omega_s^{n+1}$  to  $\Omega_s^n$  through the following discrete mapping,  $\mathbf{X}_{s,h_s}^{m,n} : \Omega_s^m \rightarrow \Omega_s^n$  such that

$$\mathbf{X}_{s,h_s}^{m,n} := \mathbf{X}_{s,h_s}^n (\mathbf{X}_{s,h_s}^m)^{-1}, \quad (45)$$

by introducing the Jacobian  $J^{n+1,n} = \det(\mathbf{F}^{n+1,n})$ . For example, the most complicated term on the right hand side of (44), i.e.,  $R_6$ , can actually be rewritten as follows in an exact fashion,

$$R_6 = (\Delta t)^2 \sum_{k=1}^{M_s} \left( J^{n+1,n} \mathbf{G}_P^{n+1} \circ \mathbf{X}_{s,h_s}^{n,n+1} (\mathbf{I} + \Delta t \mathbf{Q}^n) \boldsymbol{\tau}_{s,h}^n (\mathbf{I} + \Delta t (\mathbf{Q}^n)^T) (\mathbf{G}_P^{n+1})^T \circ \mathbf{X}_{s,h_s}^{n,n+1}, \tilde{\boldsymbol{\phi}} \circ \mathbf{X}_{s,h_s}^{n,n+1} \right)_{e_{s,k}^n}, \quad (46)$$

where  $\mathbf{G}_P^{n+1} \circ \mathbf{X}_{s,h_s}^{n,n+1}$  and  $\tilde{\boldsymbol{\phi}} \circ \mathbf{X}_{s,h_s}^{n,n+1}$  are defined in  $\Omega_s^n$  through the discrete mapping  $\mathbf{X}_{s,h_s}^{n,n+1}$ , although both  $\mathbf{G}_P^{n+1}$  and  $\tilde{\boldsymbol{\phi}}$  belong to  $\boldsymbol{\Upsilon}_{h_s}^{n+1}$  ( $n = 0, 1, \dots, N-1$ ) which is constructed using the same finite elements as for  $\boldsymbol{\Upsilon}_{h_s}^0$  based on the Lagrangian mapping  $\mathbf{X}_{s,h_s}(t)$  all the time. Other less complicated terms on the right hand side of (44) can also be similarly transformed to the integral form in  $\Omega_s^n$  as well.

## 5. Numerical algorithms

It is obvious that (33) is highly nonlinear due to the nonlinear convection term of the fluid, the updated Lagrangian-based deviatoric stress of the structure  $\boldsymbol{\tau}_{s,h}^{n+1}$  as shown in (34), the unknown contact force  $f_{s,C_w}$  that depends on the normal structural stress over the unknown contacting surface  $\Gamma_C^t$ , as well as the updating structural domain that solely depends on the structural velocity all the time. In the following, we describe in Algorithm 5.1 how the developed UFMFD-FEM is implemented for the presented FSCI model by means of the Newton's linearization for handling nonlinear fluid convection and structural stress terms, and by means of the fixed-point iteration for updating the structural domain and computing the contact force when exists.

**Algorithm 5.1.** *The overall algorithm of implementing UFMFD-FEM for FSCI problems.*

1. *Initialization of the time marching. Set the time step  $n = 0$  and let  $\mathbf{v}_h^0 = \prod_h \mathbf{v}(\mathbf{x}, 0) \in \mathbf{V}_h$ ,  $p_h^0 = 0$ ,  $\boldsymbol{\tau}_{s,h}^0 = \mathbf{0}$ .  $\Omega$  and  $\Omega_s^0$  are triangulated as  $\mathcal{T}_h$  and  $\mathcal{T}_{h_s}^0$ , respectively.*
2. *Call Algorithm 5.2 to carry out the fixed-point iteration for the structural collision determination and Newton's linearization iteration for solving the entire FSCI system at the  $(n+1)$ -th time step ( $n \geq 0$ ).*
3. *Update the discrete deviatoric stress of the structure,  $\boldsymbol{\tau}_{s,h}^{n+1}$ , by means of (43) and (44).*
4. *Time marching. If  $n+1 < N$ , then set  $n+1$  to  $n$ , go back to Step 2 and continue the time marching. Otherwise, stop the entire computation.*

Next, we carry out the following structural collision algorithm to determine the repulsive contact force  $f_{s,C_w}^{n+1}$  and the contacting surface  $\Gamma_C^{n+1}$  between the structure and fluidic channel wall at the  $(n+1)$ -th time step.

**Algorithm 5.2.** *The nonlinear iteration algorithm for structural collision determination at the  $(n+1)$ -th time step.*

1. *Initialization of the fixed-point iteration for collision determination. Set  $k = 0$ , let  $(\mathbf{v}_h^{n+1,0}, p_h^{n+1,0}) = (\mathbf{v}_h^n, p_h^n)$  and  $f_{s,C_w}^{n+1,0} = 0$  be the initial guess of the fixed-point iteration at the  $(n+1)$ -th time step ( $n \geq 0$ ). Let  $\varepsilon$  be a given tolerance.*
2. *Call Algorithm 5.3 to carry out the Newton's linearization for solving the FSCI system at the  $(n+1)$ -th time step and the  $(k+1)$ -th fixed-point iteration step, and obtain the desired numerical solution  $(\mathbf{v}_h^{n+1,k+1}, p_h^{n+1,k+1})$ , including the structural velocity  $\mathbf{v}_{h_s}^{n+1,k+1} \circ \mathbf{X}_{s,h_s}^{n,n+1} = \mathbf{v}_h^{n+1,k+1}|_{\Omega_s^n}$  by (40) and the structural mesh  $\mathcal{T}_{h_s}^{n+1,k+1}$  by (41).*
3. *To determine  $\Gamma_C^{n+1,k+1}$ , we first introduce a fluidic boundary layer whose boundary is  $\partial\Omega \cup \Gamma_h^{BL}$  and whose triangulation is  $\mathcal{T}_h^{BL} \subset \mathcal{T}_h$  along the fluidic channel wall  $\partial\Omega$ , as illustrated in Figure 4, where  $\mathcal{T}_h^{BL}$  might be the*

first two-layer fluidic elements within the boundary layer that is attached to  $\partial\Omega$  and bounded by  $\Gamma_h^{BL}$ . Then, let  $\mathcal{T}_{h_s}^{n+1,k+1}(\partial\Omega_s)$  be a partition of  $\partial\Omega_s^{n+1,k+1}$  associated with  $\mathcal{T}_{h_s}^{n+1,k+1}$ , and define

$$\Gamma_C^{n+1,k+1} = \left\{ e \in \mathcal{T}_{h_s}^{n+1,k+1}(\partial\Omega_s) : e \cap \mathcal{T}_h^{BL} \neq \emptyset \right\}, \quad (47)$$

as sketched by red line segments in Figure 4 over the structural surface.

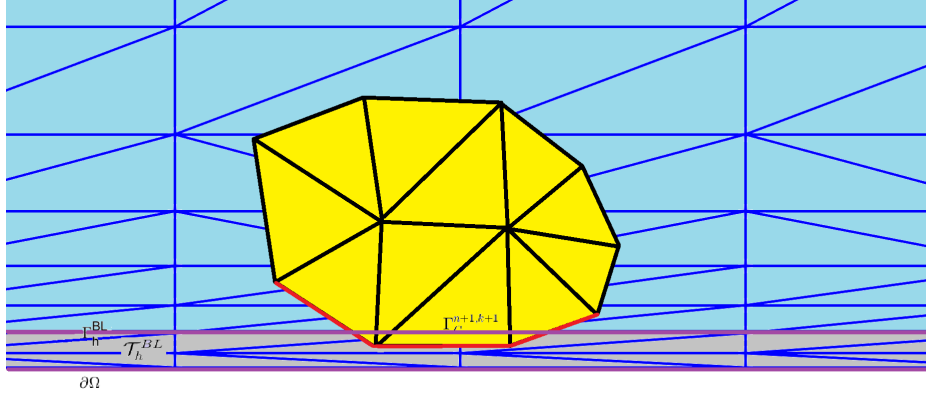


Figure 4: A schematic background fluidic and foreground structural mesh portion near the fluidic channel wall (the bottom purple line) and the approaching structure (the yellow area), which indicates the boundary-layer mesh  $\mathcal{T}_h^{BL}$  (the grey area) that is overlapped by the structural mesh, and the contacting structural surface elements  $\Gamma_C^{n+1,k+1}$  that are marked in red line segments.

4. If  $\Gamma_C^{n+1,k+1} = \emptyset$ , or  $\mathbf{v}_{h_s}^{n+1,k+1} \cdot \mathbf{n}|_{\Gamma_C^{n+1,k+1}} < \varepsilon$ , then stop the fixed-point iteration, take all obtained numerical solutions as the desired ones at the  $(n+1)$ -th time step, and exit the collision algorithm. Otherwise, go to Step 5.
5. Determine  $f_{s,C_W}^{n+1,k+1}$  by

$$f_{s,C_W}^{n+1,k+1} = \max \left\{ \zeta \frac{m_s}{\Delta t A(\Gamma_C^{n+1,k+1})} \mathbf{v}_{h_s}^{n+1,k+1} \cdot \mathbf{n} + f_{s,C_W}^{n+1,k}, 0 \right\}, \text{ on } \Gamma_C^{n+1,k+1}, \quad (48)$$

where  $f_{s,C_W}^{n+1,k+1}$  is defined as a piecewise constant function on  $\Gamma_C^{n+1,k+1}$ ,  $\zeta$  is a tunable positive dimensionless constant,  $m_s$  denotes the mass of structure, and  $A(\Gamma_C^{n+1,k+1})$  the measure of contacting surface  $\Gamma_C^{n+1,k+1}$ .

6. Set  $k+1$  to  $k$ , go back to Step 2 with the updated  $\Gamma_C^{n+1,k}$  and  $f_{s,C_W}^{n+1,k}$  in (49) to continue the fixed-point iteration.

**Remark 5.1.** In Algorithm 5.2, when the structural boundary node enters  $\mathcal{T}_h^{BL}$ , a nonlinear iteration is triggered to prevent the structural boundary node from penetrating the fluidic boundary layer as well as the fluidic channel wall. In the process of this nonlinear iteration, the magnitude of repulsive contact force increases until it is large enough to make the velocity at this boundary node in the outward normal direction is very small or negative. We point out that (48) and the stopping criteria in Step 4 of this algorithm can be viewed as a numerical implementation of the complementary contact condition (9).

When calling Algorithm 5.2 in Step 2 of Algorithm 5.1, we need to iteratively call Algorithm 5.3 in Step 2 of Algorithm 5.2 to solve (33) by virtue of Newton's linearization, as shown below.

**Algorithm 5.3.** Newton's linearization algorithm for UFMFD-FEM at the  $(n+1)$ -th time step and the  $(k+1)$ -th fixed-point iteration step.

1. Initialization of the nonlinear iteration. Let  $(\mathbf{v}_h^{n+1,k+1,0}, p_h^{n+1,k+1,0}) = (\mathbf{v}_h^{n+1,k}, p_h^{n+1,k})$  be the initial guess at the  $(n+1)$ -th time step ( $n \geq 0$ ) and the  $(k+1)$ -th fixed-point iteration step ( $k \geq 0$ ). If  $k = 0$ , let  $(\mathbf{v}_h^{n+1,0}, p_h^{n+1,0}) = (\mathbf{v}_h^n, p_h^n)$ .
2. Solve the linearized UFMFD-FEM at the  $(m+1)$ -th iteration step for  $(\mathbf{v}_h^{n+1,k+1,m+1}, p_h^{n+1,k+1,m+1}) \in \mathbf{V}_h \times W_h$  such that

$$\left\{ \begin{aligned}
& \left( \rho_f \frac{\mathbf{v}_h^{n+1,k+1,m+1} - \mathbf{v}_h^n}{\Delta t}, \tilde{\mathbf{v}}_h \right)_\Omega + (\rho_f \mathbf{v}_h^{n+1,k+1,m} \cdot \nabla \mathbf{v}_h^{n+1,k+1,m+1}, \tilde{\mathbf{v}}_h)_\Omega + (\rho_f \mathbf{v}_h^{n+1,k+1,m+1} \cdot \nabla \mathbf{v}_h^{n+1,k+1,m}, \tilde{\mathbf{v}}_h)_\Omega \\
& + 2 \left( \mu_f \mathbf{D}(\mathbf{v}_h^{n+1,k+1,m+1}), \mathbf{D}(\tilde{\mathbf{v}}_h) \right)_\Omega - \left( p_h^{n+1,k+1,m+1}, \nabla \cdot \tilde{\mathbf{v}}_h \right)_\Omega - \left( \nabla \cdot \mathbf{v}_h^{n+1,k+1,m+1}, \tilde{p}_h \right)_\Omega \\
& + \left( (\rho_s - \rho_f) \frac{\mathbf{v}_h^{n+1,k+1,m+1}|_{\Omega_s^n} - \mathbf{v}_h^n|_{\Omega_s^n}}{\Delta t}, \tilde{\mathbf{v}}_h|_{\Omega_s^n} \right)_{\Omega_s^n} + \left( \bar{\boldsymbol{\tau}}_{s,h}^{n+1,k+1,m+1}, \nabla_{\mathbf{x}^n} \tilde{\mathbf{v}}_h|_{\Omega_s^n} \right)_{\Omega_s^n} \\
& - 2 \left( \mu_f \mathbf{D}(\mathbf{v}_h^{n+1,k+1,m+1}|_{\Omega_s^n}), \mathbf{D}(\tilde{\mathbf{v}}_h|_{\Omega_s^n}) \right)_{\Omega_s^n} - \sum_{j=1}^M \xi_j \left( \mathbf{R}_h^{n+1,k+1,m+1}, \nabla \tilde{p}_h \right)_{e_j} \\
& = (\rho_f \mathbf{v}_h^{n+1,k+1,m} \cdot \nabla \mathbf{v}_h^{n+1,k+1,m}, \tilde{\mathbf{v}}_h)_\Omega + \mu_s (\Delta t)^2 \left( \nabla_{\mathbf{x}^n} \mathbf{v}_h^{n+1,k+1,m}|_{\Omega_s^n} \left( \nabla_{\mathbf{x}^n} \mathbf{v}_h^{n+1,k+1,m}|_{\Omega_s^n} \right)^T, \nabla_{\mathbf{x}^n} \tilde{\mathbf{v}}_h|_{\Omega_s^n} \right)_{\Omega_s^n} \\
& - \left( \boldsymbol{\tau}_{s,h}^n, \nabla_{\mathbf{x}^n} \tilde{\mathbf{v}}_h|_{\Omega_s^n} \right)_{\Omega_s^n} + (\Delta t)^2 \left( \nabla_{\mathbf{x}^n} \mathbf{v}_h^{n+1,k+1,m}|_{\Omega_s^n} \boldsymbol{\tau}_{s,h}^n \left( \nabla_{\mathbf{x}^n} \mathbf{v}_h^{n+1,k+1,m}|_{\Omega_s^n} \right)^T, \nabla_{\mathbf{x}^n} \tilde{\mathbf{v}}_h|_{\Omega_s^n} \right)_{\Omega_s^n} \\
& + (\rho_f \mathbf{g}, \tilde{\mathbf{v}}_h)_\Omega + \left( (\rho_s - \rho_f) \mathbf{g}, \tilde{\mathbf{v}}_h|_{\Omega_s^n} \right)_{\Omega_s^n} + \langle \mathbf{f}_{f,N}^{n+1}, \tilde{\mathbf{v}}_h \rangle_{\partial \Omega_{f,N}^{n+1}} - \langle f_{s,C_W}^{n+1,k}, \tilde{\mathbf{v}}_h|_{\Gamma_C^{n+1,k}} \cdot \mathbf{n} \rangle_{\Gamma_C^{n+1,k}},
\end{aligned} \right. \quad (49)$$

$\forall (\tilde{\mathbf{v}}_h, \tilde{p}_h) \in \mathbf{V}_{0,h} \times W_h, \quad m = 0, 1, 2, \dots,$

where

$$\begin{aligned}
\bar{\boldsymbol{\tau}}_{s,h}^{n+1,k+1,m+1} &= \mu_s \Delta t \left( \nabla_{\mathbf{x}^n} \mathbf{v}_h^{n+1,k+1,m+1}|_{\Omega_s^n} + \left( \nabla_{\mathbf{x}^n} \mathbf{v}_h^{n+1,k+1,m+1}|_{\Omega_s^n} \right)^T \right) \\
&+ \Delta t \nabla_{\mathbf{x}^n} \mathbf{v}_h^{n+1,k+1,m}|_{\Omega_s^n} \left( \nabla_{\mathbf{x}^n} \mathbf{v}_h^{n+1,k+1,m+1}|_{\Omega_s^n} \right)^T + \Delta t \nabla_{\mathbf{x}^n} \mathbf{v}_h^{n+1,k+1,m+1}|_{\Omega_s^n} \left( \nabla_{\mathbf{x}^n} \mathbf{v}_h^{n+1,k+1,m}|_{\Omega_s^n} \right)^T \\
&+ \Delta t \nabla_{\mathbf{x}^n} \mathbf{v}_h^{n+1,k+1,m+1}|_{\Omega_s^n} \boldsymbol{\tau}_{s,h}^n + \Delta t \boldsymbol{\tau}_{s,h}^n \left( \nabla_{\mathbf{x}^n} \mathbf{v}_h^{n+1,k+1,m+1}|_{\Omega_s^n} \right)^T \\
&+ (\Delta t)^2 \nabla_{\mathbf{x}^n} \mathbf{v}_h^{n+1,k+1,m}|_{\Omega_s^n} \boldsymbol{\tau}_{s,h}^n \left( \nabla_{\mathbf{x}^n} \mathbf{v}_h^{n+1,k+1,m+1}|_{\Omega_s^n} \right)^T \\
&+ (\Delta t)^2 \nabla_{\mathbf{x}^n} \mathbf{v}_h^{n+1,k+1,m+1}|_{\Omega_s^n} \boldsymbol{\tau}_{s,h}^n \left( \nabla_{\mathbf{x}^n} \mathbf{v}_h^{n+1,k+1,m}|_{\Omega_s^n} \right)^T,
\end{aligned} \quad (50)$$

$$\mathbf{R}_h^{n+1,k+1,m+1} = \rho_f \frac{\mathbf{v}_h^{n+1,k+1,m+1} - \mathbf{v}_h^n}{\Delta t} + \rho_f \mathbf{v}_h^{n+1,k+1,m} \cdot \nabla \mathbf{v}_h^{n+1,k+1,m+1} + \nabla p_h^{n+1,k+1,m+1} - \rho_f \mathbf{g}, \quad (51)$$

$$\xi_j = \left[ \left( \zeta_0 \frac{\rho_f}{\Delta t} \right)^2 + \left( \zeta_1 \frac{\mu_f}{h_j^2} \right)^2 + \left( \zeta_2 \frac{\rho_f \|\mathbf{v}_h^{n+1,k+1,m}\|}{h_j} \right)^2 \right]^{-\frac{1}{2}}, \quad 1 \leq j \leq M. \quad (52)$$

3. Check the stopping criteria for the nonlinear iteration. Stop the iteration if

$$\|\mathbf{v}_h^{n+1,k+1,m+1} - \mathbf{v}_h^{n+1,k+1,m}\|_0 + \|p_h^{n+1,k+1,m+1} - p_h^{n+1,k+1,m}\|_0 \leq \varepsilon,$$

where  $\varepsilon$  is a given tolerance, set  $(\mathbf{v}_h^{n+1,k+1}, p_h^{n+1,k+1}) = (\mathbf{v}_h^{n+1,k+1,m+1}, p_h^{n+1,k+1,m+1})$ , update the structural domain  $\Omega_s^{n+1,k+1}$  and its updated Lagrangian mesh  $\mathcal{T}_{h_s}^{n+1,k+1}$  by (40) and (41), and stop the nonlinear iteration. Otherwise, set  $m+1$  to  $m$ , go back to Step 2 and continue the nonlinear iteration.

## 6. Numerical experiments

In this section, we validate numerical performances of the developed UFMFD-FEM via two benchmark FSI problems first: the particulate fluid of (1) the simple shear flow type; and (2) the plane Poiseuille flow type, then via a self-defined small-scale DLD problem second, finally via a realistic large-scale DLD problem by comparing with its physical experiments, where the particle collision with tilted pillar arrays inside the microfluidic channel are engaged in the fluid flow.

### 6.1. Example 1: The simple shear flow-particle interaction benchmark problem

First, we consider the case of a neutrally buoyant particle of circular shape locating at the middle of the fluidic channel between two walls. This example was considered by Pan et al. in [42], where the distributed Lagrange multiplier/fictitious domain (DLM/FD) method was employed to solve the problem. Here we use the same sets of parameters as in [42] to validate our proposed UFMFD-FEM that produces very similar results with those in [42], as shown below.

As illustrated in the left part of Figure 5, the computational domain  $\Omega := [0, 2] \times [0, 2]$ , and the mass center of the circular particle locates at  $(1, 1)$ . The periodic velocity boundary condition is defined on the left and right boundary,  $\Gamma_P^f$ , and the shear flow condition is assigned to the top boundary as  $\mathbf{v}_f|_{\Gamma_{D,1}^f} = (\frac{\gamma H}{2}, 0) = (1, 0)^T$  and to the bottom boundary as  $\mathbf{v}_f|_{\Gamma_{D,2}^f} = (-\frac{\gamma H}{2}, 0) = (-1, 0)^T$ , respectively, where  $\gamma$  denotes the shear rate of the fluid with the fixed value  $\gamma = 1$  ( $\text{s}^{-1}$ ), and  $H = 2$  is the distance between the top and bottom walls. We introduce the confined ratio

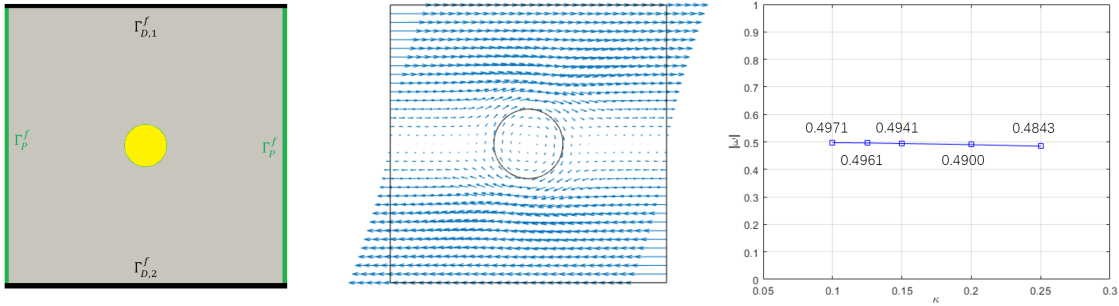


Figure 5: The simple shear flow-particle interaction problem: the computational domain (left); the velocity field of the case  $\kappa = 0.2$  (middle); the angular speed  $|\omega|$  versus the confined ratio  $\kappa$  (right).

defined as  $\kappa = 2r/H$ , where  $r$  is the radius of circular particle. Thus  $\kappa = r$  in this example. Further, we take the fluid viscosity as  $\mu_f = 1$ , and densities of both the fluid and particle as  $\rho_f = \rho_s = 1$ . Finally, different from [42] where the initial condition of fluid velocity is defined by a simple shear flow associated with the given shear rate without particle, here we treat the initial velocity field of both the fluid and particle at rest.

Under the shear flow condition, it is known that the relationship between the angular velocity and rotational angle of an elliptic shape particle in an unbounded shear flow is given as follows according to Jeffery's solution [26]

$$\omega = -\gamma \frac{r_a^2 \sin^2 \theta + r_b^2 \cos^2 \theta}{r_a^2 + r_b^2}, \quad (53)$$

which shows that the angular velocity is related with the ratio of  $r_a$  and  $r_b$ , theoretically, and is independent of their specific values. Nevertheless, the values of  $r_a$  and  $r_b$  used in the numerical experiment should be as small as possible as Jeffery's solution is derived under the assumption that the range of the domain is much larger than the particle size so that to minimize the fluid-particle interaction effect. Hence in this example, the Jeffery's exact solution of the angular speed of a circular particle is  $|\omega| = |-\gamma/2| = 0.5$  in an unbounded shear flow field. In our numerical

experiments below, we let the confined ratio  $\kappa$  (thus the radius of particle  $r$ ) vary from 0.1 to 0.25 to see its influence on the numerical angular speed.

In contrast to the rigid particle that is used in this benchmark problem, our structural equation (3) defined in the presented FSCI model however belongs to an incompressible neo-Hookean material. To make an elastic structure approximate to a rigid body at utmost, we can choose a sufficiently large shear modulus,  $\mu_s$ , in the constitutive relation of the elastic structure. Now we are able to carry out the developed UFMFD-FEM through Algorithm 5.3 without considering the structure collision effect to solve this benchmark problem for its numerical angular speed  $|\omega_h|$ , by taking the time step size  $\Delta t = 0.001$ ,  $m = 1$  in (32), and  $\zeta_0 = 2$ ,  $\zeta_1 = 12$  and  $\zeta_2 = 2$  as pressure stabilization parameters in (36).

We first investigate the influences of increasing shear modulus  $\mu_s$  and decreasing mesh size  $h$  on the angular speed for a circular particle with a fixed radius of 0.2, and the obtained numerical results are shown in Table 1, where we can see that for each chosen  $\mu_s$ , the corresponding numerical angular speed,  $|\omega_h|$ , becomes stably more accurate towards 0.5 along with the decreasing  $h$ , showing a stable convergence with respect to the mesh size  $h$  for our developed method. In addition, amongst three chosen shear moduli,  $\mu_s = 10^8$  (Pa) seems large enough to deliver an accurate angular speed especially for a smaller mesh size  $h$ . On the other hand, we also see from numerical computations that a much larger  $\mu_s$  may possibly make Newton's nonlinear iteration described in Algorithm 5.3 harder to converge. Therefore under the consideration of both accuracy and efficiency, a reasonably large shear modulus such as  $\mu_s = 10^8$  (Pa) shall be a good choice for the simulation of fluid-rigid particle interactions by means of our proposed FSI model and UFMFD-FEM, in practice. A snapshot of the velocity field in the case of  $\kappa = r = 0.2$  is also illustrated in the middle part of Figure 5.

Table 1: Numerical angular speeds of a circular particle with a radius of 0.2 on refining meshes under different shear moduli.

Mesh Size $h$	Shear Modulus $\mu_s$	Angular Speed $ \omega_h $
$\frac{1}{32}$	$10^6$	0.488623
	$10^8$	0.487293
	$10^{10}$	0.487285
$\frac{1}{64}$	$10^6$	0.489294
	$10^8$	0.489108
	$10^{10}$	0.489107
$\frac{1}{128}$	$10^6$	0.490046
	$10^8$	0.490028
	$10^{10}$	0.490038

Hence next, we take  $h = 1/128$ ,  $\Delta t = 0.001$  and  $\mu_s = 10^8$  to investigate the influence of the confined ratio  $\kappa$  on the numerical angular speed. The right part of Figure 5 illustrates the relationship of angular speeds versus the confined ratios, where we can see that numerical angular speeds turn to well agree with the Jeffery's solution along with decreasing particle sizes. Note that relative errors on the numerical angular speed for the cases of particle's radii  $r = 0.1, 0.125$  and  $0.15$  are less than or equal to 1%, while they become larger with increasing radius of the circular particle, which can be ascribed to the increasingly subtle influence of fluid-particle interaction effect due to the increasing particle size.

Finally, to investigate the numerical convergence rate between the obtained numerical solutions  $(\mathbf{v}_h, p_h)$  and real solutions  $(\mathbf{v}, p)$  that are impossibly prescribed for the studied benchmark problem, we conduct an error estimate based upon numerical solutions on a sequence of nested meshes with the mesh sizes  $2^j h$ ,  $j = 0, 1, 2, \dots$  as follows,  $\|\phi_{2^j h} - \phi_{2^{j+1} h}\|_{L^2(\Omega)} \leq \|\phi - \phi_{2^j h}\|_{L^2(\Omega)} + \|\phi - \phi_{2^{j+1} h}\|_{L^2(\Omega)}$ , which is under the circumstance that our proposed numerical scheme converges to the real solution of the benchmark problem, and here  $\phi$  can be  $\mathbf{v}$  or  $p$ . Then, while  $\Delta t$

is sufficiently small, apply (37) to two adjacent mesh levels with the mesh size  $2^j h$  and  $2^{j+1} h$ , respectively, yields

$$\|\mathbf{v}_{2^j h} - \mathbf{v}_{2^{j+1} h}\|_{L^2(\Omega)^d} = O(2^{(j+1)r} h^r), \quad \|p_{2^j h} - p_{2^{j+1} h}\|_{L^2(\Omega)} = O(2^{(j+1)q} h^q), \quad \text{for } 1 < r \leq 3/2, \quad 0 < q \leq 1/2.$$

Thus, we have the following numerical convergence rate indicators of the velocity and pressure attained on every three adjacent mesh levels,

$$\frac{\|\mathbf{v}_{2^{j+1} h} - \mathbf{v}_{2^{j+2} h}\|_{L^2(\Omega)^d}}{\|\mathbf{v}_{2^j h} - \mathbf{v}_{2^{j+1} h}\|_{L^2(\Omega)^d}} = 2^r, \quad \frac{\|p_{2^{j+1} h} - p_{2^{j+2} h}\|_{L^2(\Omega)}}{\|p_{2^j h} - p_{2^{j+1} h}\|_{L^2(\Omega)}} = 2^q, \quad (54)$$

which demonstrate the  $r$ th-order convergence rate of velocity in  $L^2$  norm and the  $q$ th-order convergence rate of pressure in  $L^2$  norm as well, where  $1 < r \leq 3/2$  and  $0 < q \leq 1/2$ .

Applying (54) to numerical results of the developed UFMFD-FEM obtained for the benchmark problem on every three adjacent meshes of the aforementioned mesh doubling, we eventually gain numerical convergence rates of the velocity and pressure as shown in Table 2, where the convergence errors  $\|\mathbf{v}_{2^{j-1} h} - \mathbf{v}_{2^j h}\|_{L^2(\Omega)^d}$  and  $\|p_{2^{j-1} h} - p_{2^j h}\|_{L^2(\Omega)}$  with  $h = 1/256$  and  $j = 3, 2, 1$ , reversely, are indeed reduced by factors of at least  $2^{3/2}$  and of at least  $2^{1/2}$  (indicated by values in columns labeled ‘‘Ratio’’), respectively, for each doubling of resolution. Thus, we can conclude that the obtained numerical solutions are accurate by holding the convergence rates of order  $\frac{3}{2}$  and of order  $\frac{1}{2}$  in  $L^2$  norm for velocity and pressure, respectively, which are consistent with the supposed numerical convergence property (37) and the associated convergence rate indicators (54).

Table 2: Convergence errors & rates of velocity and pressure on successively nested grids for Example 1

Mesh Sizes		Velocity		Pressure	
$j$	$2^j h$	$\ \mathbf{v}_{2^{j-1} h} - \mathbf{v}_{2^j h}\ _{L^2(\Omega)^d}$	Ratio	$\ p_{2^{j-1} h} - p_{2^j h}\ _{L^2(\Omega)}$	Ratio
3	1/32	$2.4000 \times 10^{-2}$	2.62	$2.1471 \times 10^{-1}$	1.67
2	1/64	$9.1558 \times 10^{-3}$	3.50	$1.2864 \times 10^{-1}$	1.56
1	1/128	$2.6157 \times 10^{-3}$	—	$8.2492 \times 10^{-2}$	—
0	1/256	—	—	—	—

## 6.2. Example 2: The plane Poiseuille flow-particle interaction benchmark problem

In the second example, we consider to simulate the motion of a neutrally buoyant rigid particle in a pressure-driven Poiseuille flow, which was studied by Pan et al. in [41] using the DLM/FD method as well, and also by Inamuro et al. in [25] via the lattice Boltzmann method. Here we employ the same sets of parameters as in [41] to validate our developed UFMFD-FEM. As shown in Figure 6(a), the computational domain is  $\Omega := [0, 1] \times [0, 1]$  (i.e.,  $L = 1$ ), where the periodic- and no-slip velocity boundary conditions are assigned to the left and right boundary,  $\Gamma_P^f$ , and to the top and bottom boundary,  $\Gamma_D^f$ , respectively. In addition, to drive the fluid flow from the left to the right, we introduce a pressure drop,  $\Delta p$  (Pa), to this example which is equivalent with a compound Neumann (stress) boundary condition on  $\Gamma_P^f$ , and, we take  $\Delta p$  as variable values in different testing cases (see Table 3). The fluidic and particle velocities are set as zero, initially, i.e.,  $\mathbf{v}_f^0 = \mathbf{v}_s^0 = 0$ , the circular particle’s diameter is taken as 0.25, and its center’s vertical coordinate as  $y_c = 0.4$ , initially. Densities of the fluid and the particle are the same and both are set as 1, and, the fluid viscosity  $\mu_f$  (kg/m/s) varies as well in different testing cases (see Table 3). Again, we take the structural shear modulus  $\mu_s = 10^8$  (Pa), and employ Algorithm 5.3 to solve this benchmark problem, where the pressure-stabilized  $P_1/P_1$  mixed finite element is adopted with well tuned stabilization parameters, as chosen in Section 6.1.

Table 3: Parameters and numerical results in six testing cases compared with [41] denoted as [•].

Test#	$\mu_f$	$\Delta p$	$[\bar{u}]$	$\bar{u}$	$[y_c]$	$y_c$	$[\omega]$	$\omega$
1	$3.2498036 \times 10^{-3}$	$1.763 \times 10^{-3}$	0.04155	0.04131	0.2732	0.2735	-0.05345	-0.05315
2	$1.5000000 \times 10^{-3}$	$8.167 \times 10^{-4}$	0.04159	0.04141	0.2725	0.2731	-0.05343	-0.05304
3	$9.4984908 \times 10^{-4}$	$5.133 \times 10^{-4}$	0.04122	0.04104	0.2723	0.2727	-0.05264	-0.05215
4	$7.5000000 \times 10^{-4}$	$4.100 \times 10^{-4}$	0.04166	0.04146	0.2720	0.2724	-0.05283	-0.05222
5	$6.0000000 \times 10^{-4}$	$3.270 \times 10^{-4}$	0.04148	0.04114	0.2719	0.2723	-0.05206	-0.05135
6	$4.2834760 \times 10^{-4}$	$2.337 \times 10^{-4}$	0.04144	0.04116	0.2722	0.2728	-0.05052	-0.04962

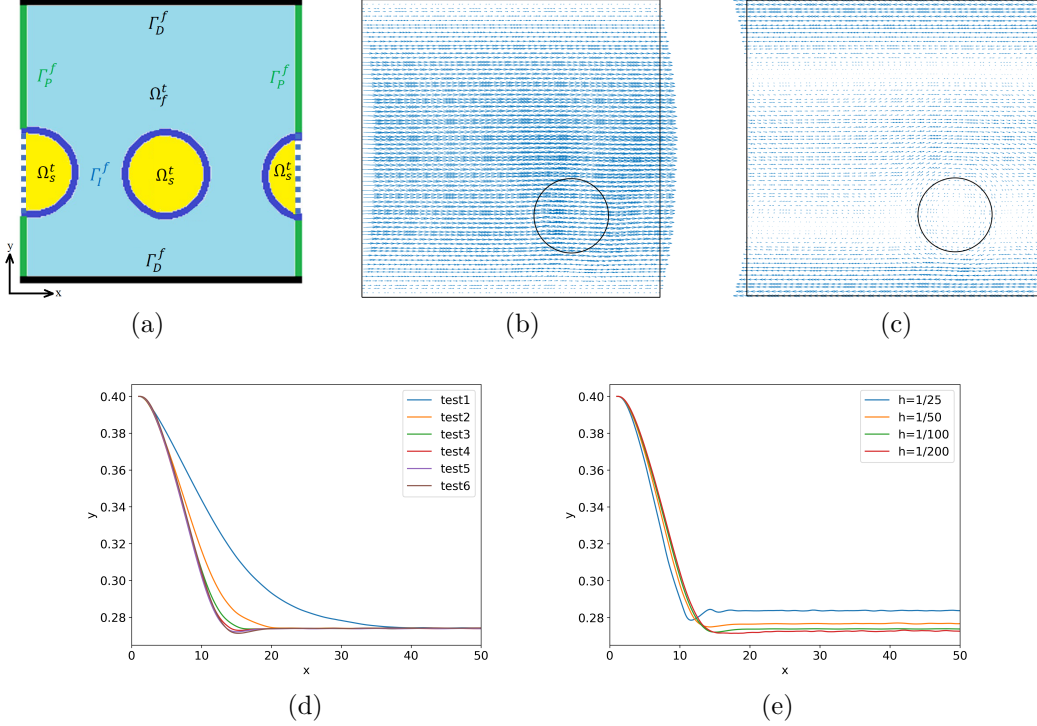


Figure 6: The plane Poiseuille flow-particle interaction problem: (a) the computational domain with the length  $L = 1$ ; (b) the total velocity field at the equilibrium position in Test #5; (c) the rotating velocity field surrounding the particle at the equilibrium position in Test #5 after an average (translational) velocity of the particle is deducted from the total velocity field; (d) lateral migrations of a circular particle in different tests; (e) lateral migrations of a circular particle with different mesh sizes in Test #5.

First of all, we fix  $h = 1/200$  and let  $\Delta t = 0.05$  before the particle reaches the equilibrium position, thereafter  $\Delta t = 0.002$ , as chosen in [41]. The obtained numerical results of six testing cases with different values of pressure drop and of fluid viscosity as used in [41] are shown in Table 3, where the space-averaged inlet velocity  $\bar{u}$  (m/s), the equilibrium position and angular velocity of the circular particle,  $y_c$  (m) and  $\omega$  (rad/s), are listed and hold the relative errors from corresponding results in [41] (denoted as  $[\bar{u}]$ ,  $[y_c]$  and  $[\omega]$  in Table 3) between 0.43% ~ 0.82%, 0.11% ~ 0.22%, and 0.56% ~ 1.78%, respectively, illustrating that the particle's angular velocity  $\omega$  is influenced by Reynolds numbers of the fluid ( $Re = \rho_f \bar{u} L / \mu_f$ ) the most, and, its relative errors even increase along with Reynolds numbers, whereas the particle's equilibrium position  $y_c$  possesses the smallest error range and is thus affected by Reynolds numbers the least. The same fact is also displayed in Figure 6(d), where we can see all lateral migration curves of the evolving particle, which start from the same initial position in six testing cases, eventually approach to the same equilibrium position, resulting in the following phenomenon that the equilibrium state of the evolving particle is independent of Reynolds numbers of the plane Poiseuille flow. Figure 6(b) shows a snapshot of velocity field at the equilibrium position in Test #5, illustrating that the particle mainly conducts a translational motion due to the horizontal fluid flow driven by the pressure drop from the left to the right. To show the particle also does a

slightly rotational motion at the same time in Test #5, we first calculate an average velocity over totally  $N_s$  mesh nodes of the particle with an equal weight  $1/N_s$ , which can be considered as an approximation to the translational velocity of the rigid particle. Then, we subtract such an average velocity of the particle from the velocity field shown in Figure 6(b) to obtain a clockwise rotational velocity field (the angular velocity is thus negative) surrounding the center of particle as shown in Figure 6(c), and, the rotational velocity field fades away as approaching to the center of particle, showing a decreasing rotational velocity field along the radius direction that is nearly anti-proportional to the distance from the center of particle.

Next, to investigate the convergence property of our proposed method on this example, without loss of generality, we pick Test #5 in particular, and produce a series of successively nested meshes with  $h = \frac{1}{25}, \frac{1}{50}, \frac{1}{100}, \frac{1}{200}$ , on which we carry out Algorithm 5.3 for Test #5 with the time step size  $\Delta t = 0.002$  to gain numerical solutions, respectively. Then, as done in Section 6.1, we investigate the numerical convergence rate between the obtained numerical solutions  $(\mathbf{v}_h, p_h)$  and the real solution  $(\mathbf{v}, p)$  by checking if (54) still holds amongst every three adjacent mesh levels for this benchmark problem. As Table 4 shows, we observe that the convergence errors  $\|\mathbf{v}_{2^{j-1}h} - \mathbf{v}_{2^j h}\|_{L^2(\Omega)^d}$  and  $\|p_{2^{j-1}h} - p_{2^j h}\|_{L^2(\Omega)}$  with  $h = 1/200$  and  $j = 3, 2, 1$ , reversely, are still roughly reduced by factors of  $2^{3/2}$  and of  $2^{1/2}$  or so, respectively, for each doubling of resolution, illustrating that numerical solutions of the benchmark problem still roughly hold the convergence rates of order  $\frac{3}{2}$  and of order  $\frac{1}{2}$  in  $L^2$  norm for velocity and pressure, respectively, which agree with the supposed numerical convergence property (37) and the associated convergence rate indicators (54), again. On the

Table 4: Convergence errors & rates of velocity and pressure on successively nested grids for Example 2

Mesh Sizes		Velocity		Pressure	
$j$	$2^j h$	$\ \mathbf{v}_{2^{j-1}h} - \mathbf{v}_{2^j h}\ _{L^2(\Omega)^d}$	Ratio	$\ p_{2^{j-1}h} - p_{2^j h}\ _{L^2(\Omega)}$	Ratio
3	1/25	$1.7655 \times 10^{-3}$	2.57	$4.4926 \times 10^{-5}$	2.36
2	1/50	$6.8578 \times 10^{-4}$	2.14	$1.9036 \times 10^{-5}$	1.54
1	1/100	$3.2107 \times 10^{-4}$	—	$1.2399 \times 10^{-5}$	—
0	1/200	—	—	—	—

other hand, Figure 6(e) illustrates lateral migration curves of the circular particle from the same initial position over four different mesh sizes, where we can see that along with the decreasing mesh size the equilibrium states of four curves are farther away from the center axis of the fluidic channel (i.e., the horizontal line  $y = 0.5$ ) one after the other, and, the distance between every two adjacent curves' equilibrium state also keeps decreasing while the mesh size decreases, showing also an approximation process with respect to the mesh size  $h$  as well, qualitatively.

### 6.3. Example 3: A self-defined FSCI problem with particle collisions over the fluidic channel wall

In this example, we numerically test a FSCI model problem with contact effects between the structure and fluidic channel wall occurring in  $\Omega = [0, 2] \times [0, 1] \setminus (\mathcal{O}_1 \cup \mathcal{O}_2)$  (i.e.,  $L = 2, H = 1$ ), where  $\mathcal{O}_1$  and  $\mathcal{O}_2$  are two circular pillar obstacles with the same radius 0.15, and centered at (0.8, 0.4) and (1.2, 0.6), respectively, and,  $\Gamma_{\mathcal{O}} = \partial\mathcal{O}_1 \cup \partial\mathcal{O}_2$ . The structure is a circular particle with radius 0.04 that is initially positioned at (0.4, 0.57), as shown in Figure 7. Note that in this example units of length and time are micrometers ( $\mu\text{m}$ ) and microsecond (ms), respectively. All involved physical parameters are listed in Table 5.

Table 5: Symbol descriptions and values in unit for physical parameters

Symbol	Description	Value	Unit
$\rho_f$	Density of fluid	$1.005584 \times 10^{-12}$	$\text{g} \cdot \mu\text{m}^{-3}$
$\mu_f$	Viscosity of fluid	$1.0219 \times 10^{-9}$	$\text{g} \cdot \mu\text{m}^{-1} \cdot \text{ms}^{-1}$
$\rho_s$	Density of particle	$1.05 \times 10^{-12}$	$\text{g} \cdot \mu\text{m}^{-3}$
$\mu_s$	Shear modulus of particle	1	$\text{g} \cdot \mu\text{m}^{-1} \cdot \text{ms}^{-2}$

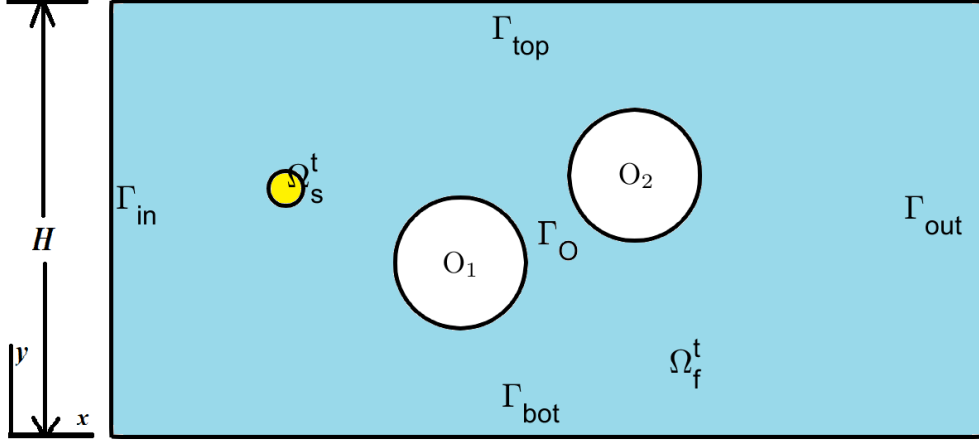


Figure 7: Computational domain of a self-defined FSCI problem.

We set zero for initial conditions of all variables in the interior domain, while subjecting to their own boundary conditions on the boundary as shown below. And, the initial structural displacement is also at rest, i.e., the particle stays still initially. As for the setup of boundary conditions, we define a parabolic profile for the incoming flow on the inlet  $\Gamma_{in}$  as follows

$$\mathbf{v}_f^{\text{in}} = (v_{f,x}^{\text{in}}, 0)^T, \text{ and, } v_{f,x}^{\text{in}} = \begin{cases} v_{\max} \frac{2y(H-y)}{H^2} \left(1 - \cos\left(\frac{\pi t}{t_0}\right)\right), & t \leq t_0 \\ v_{\max} \frac{4y(H-y)}{H^2}, & \text{otherwise,} \end{cases} \quad (55)$$

where  $v_{\max} = 1 \mu\text{m/ms}$  denotes the maximum value of parabolic incoming velocity profile,  $t_0$  is a prescribed buffer time period within which the fluid flow can be developed from its zero initial state to a stable state throughout  $\Omega_f^{t_0}$  with an increasing incoming velocity boundary condition from zero to  $\mathbf{v}_f^{\text{in}}(\mathbf{x}, t_0)$ . Additionally, the do-nothing boundary condition is applied to the outlet  $\Gamma_{out}$ , i.e.,  $\mathbf{f}_{f,N} = 0$  in (2)<sub>2</sub>, and the no-slip boundary condition (2)<sub>1</sub> with  $\mathbf{v}_{f,D} = 0$  is defined on  $\Gamma_{top} \cup \Gamma_{bot} \cup \Gamma_O$ .

As shown in Figure 8, we triangulate the entire domain  $\Omega$  with a fixed mesh  $\mathcal{T}_h$ , and the initial structure domain  $\Omega_s^0$  with a mesh  $\mathcal{T}_{h_s}^0$ , where  $\mathcal{T}_h$  consists of 9895 nodes and 19042 elements, while  $\mathcal{T}_{h_s}^0$  contains 660 nodes and 1180 elements. The time step size is taken as  $\Delta t = 0.01 \text{ ms}$ . Further, we distribute a finer fluidic boundary-layer mesh along  $\Gamma_O$  with a size  $h_C = 0.003 \mu\text{m}$ . The parameter  $\zeta$  in (48) is set to be  $10^4$ , and the tolerance  $\varepsilon$  in Step 4 of Algorithm 5.2 is chosen as  $0.001 h_C \Delta t^{-1}$ .

The lateral migration of particle is shown in Figure 9 with the field of velocity magnitude as the background, where some red parts on the trajectory of the particle's center near the right pillar illustrate that the contacting phenomena occur between the particle and the right pillar obstacle at those places. A typical contacting process at one time step obtained by Algorithm 5.2 is shown in Figure 10, where the thin lines in brown, blue, green and red colors represent the location of structural elements at the beginning of nonlinear iteration, after 10 and 20 times iteration, and at the end of (after 35 times) iteration, respectively, until no structural element falls into the fluidic boundary-layer mesh that is colored in grey and bounded by a thick purple line. In Figure 10 one can observe that, at the beginning of nonlinear iteration, some vertices of structural elements enter the fluidic boundary layer, which indicates the contacting collision between the structure and fluidic channel wall numerically occurs and thus triggers Algorithm 5.2. The repulsive contact force  $f_{s,C_W}$  and the contacting surface  $\Gamma_C^t$  are then updated and determined by the nonlinear iteration process described in Algorithm 5.2. According to (48),  $f_{s,C_W}$  is gradually increased to prevent the structure from penetrating into the fluidic boundary layer when  $\mathbf{v}_{h_s}^{n+1,k+1} \cdot \mathbf{n}|_{\Gamma_C^{n+1,k+1}}$  keeps positive. The stopping criteria of Algorithm 5.2,  $\Gamma_C^{n+1,k+1} = \emptyset$  or  $\mathbf{v}_{h_s}^{n+1,k+1} \cdot \mathbf{n}|_{\Gamma_C^{n+1,k+1}} < \varepsilon$ , together with (48) that is to update the non-negative repulsive contact force, imply that the original contact condition (9) numerically holds in an equivalent fashion. Finally, Figure 10 also

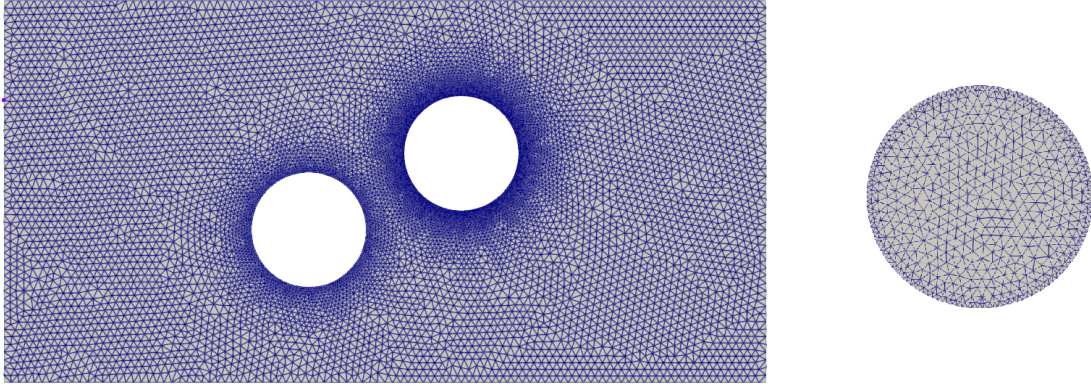


Figure 8: Meshes for  $\Omega$  (left) and  $\Omega_s^0$  (right).

illustrates that the structure is pushed away from the fluidic boundary layer as desired (shown by the thin red line) at the end of nonlinear iteration process.

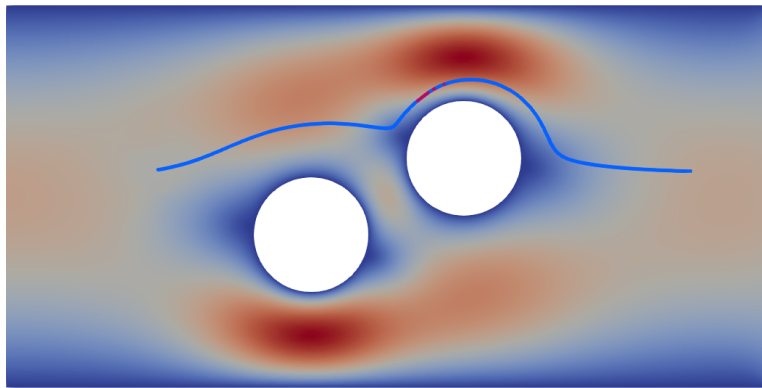


Figure 9: The lateral migration of particle with the field of velocity magnitude as the background.

#### 6.4. Example 4: A realistic particulate FSCI problem in a deterministic lateral displacement microchip

In this section, we further validate the developed UFMFD-FEM by investigating its numerical performances on a realistic particulate FSCI problem that arises from a DLD microchip. The DLD method is a robust passive microfluidic particle separation technique established by Huang et al. [21] for the first time to sort particles based on their size with pillar arrays. During the last decade, DLD has become popular and widely used for particle separation and detection by holding a promise to provide a precise particle manipulation with a high-resolution separation in a robust fashion and at low cost. The mechanism of DLD is to use arrays of offset micro-pillars within a flow channel to sort particles based on diameter in a high throughput manner. DLD mostly operates at low Reynolds numbers and provides high dynamic size separation, which ranges from millimeter to micro- and nanometer sizes. Particle flows in the DLD array are influenced by both the fluidic forces and the pillar obstacles effect. A critical size for particle separation, which is so called the DLD critical diameter denoted by  $D_c$ , is determined by the gap between the pillars and the angle of the pillar array in relation to the main direction of flow. When the particle is located in the pillar gap, the particle with a diameter smaller than  $D_c$  will follow the initial streamline and travel in the zigzag mode, while the particle larger than  $D_c$  will be bumped to the pillar and displace laterally to the next streamline, as shown in Figure 11.

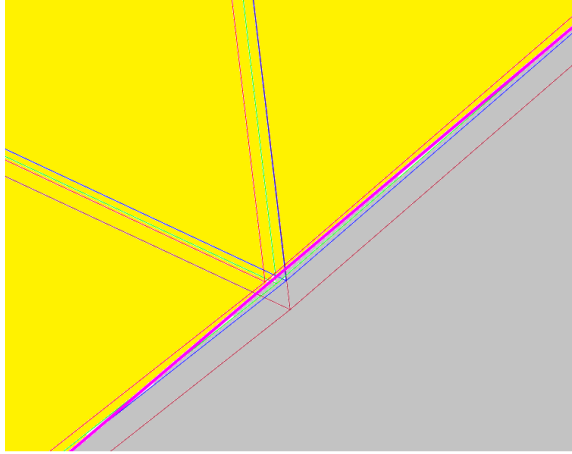


Figure 10: The nonlinear iteration process of determining the repulsive contact force: the respective location of structural elements at the beginning of the nonlinear iteration (brown line), after 10 times iteration (blue line), after 20 times iteration (green line), and the final location (red line), where the grey area is a part of the fluidic boundary-layer mesh, the yellow area is a part of the structural mesh, the thick purple line is a part of  $\Gamma_h^{BL}$  that is the boundary of first two-layer meshes from the fluidic channel wall within the fluidic boundary layer.

A two-dimensional computational domain of DLD microchip as well as its mesh triangulation are depicted in Figure 12, where a matrix of pillar obstacles, i.e., the micro-posts array that are also inner walls of the filter microfluidic channel  $\Omega_t^f$ , are built into the microchip at an oblique angle to attempt to produce an effect of particle isolation, and, such an oblique angle is particularly illustrated in the green box shown in Figure 12, where the shift distances between adjacent pillar obstacles in  $x$ - and  $y$ -direction are  $0 \mu\text{m}$  and  $7.8 \mu\text{m}$ , respectively, while the horizontal and vertical distances among adjacent pillar obstacles are  $55 \mu\text{m}$  and  $62.4 \mu\text{m}$ , respectively. The radius of each circular pillar obstacle is  $17.5 \mu\text{m}$ . In addition,  $\Omega_t^s$  denotes the particle that is plotted as a small red disk. As for the mesh triangulation, we adopt  $h = h_s = 3 \mu\text{m}$  to accommodate a large-scale domain triangulation while making a fluidic boundary-layer mesh along each pillar obstacle with a mesh size  $h_C = 0.003 \mu\text{m}$ , and, we take the time step size as  $\Delta t = 0.01\text{ms}$ . We further adopt the maximum incoming velocity on the inlet,  $v_{\max} = 50 \mu\text{m}/\text{ms}$ . Moreover, boundary conditions, initial conditions, involved physical coefficients of this example, and control parameters for handling structural collisions described in Algorithm 5.2 are all set as the same with those given in Section 6.3.

Then, we carry out Algorithm 5.1 to solve the FSCI problem occurring in the depicted DLD domain. Numerical results and their comparisons with physical experiments are shown in Figure 13, where the top row displays the lateral migration of the particle of radius  $r = 2 \mu\text{m}$ , and the bottom row shows that of the particle of radius  $r = 2.5 \mu\text{m}$ , while the left column displays the numerical results versus the physical experimental results that are shown in the right column. We can see that both the numerical and physical experimental results show a very similar lateral migration of the particle, illustrating that the particle of radius  $r = 2 \mu\text{m}$  travels in the zigzag mode along the surface of pillar obstacles while the particle of radius  $r = 2.5 \mu\text{m}$  is bumped to the pillar and displaces laterally to the next streamline without doing a zigzag move. Thus by the theory of DLD critical diameter, we know that  $4 \mu\text{m} < D_c < 5 \mu\text{m}$  in this DLD microchip, showing a good agreement between the numerical and physical experiments.

## 7. Conclusion and future work

In this paper, we develop a nonlinearly coupled system of partial differential equations for one kind of fluid-structure-contact interaction (FSCI) problem involving the interactional effect between the fluid and structure, and the collision effect between the structure and fluidic channel wall, where the structural motion may undergo large translational and rotational displacements and/or deformations. To numerically tackle such a FSCI problem, we develop a stabilized mixed finite element method within the frame of monolithic fictitious domain/immersed boundary (FD/IB) approach

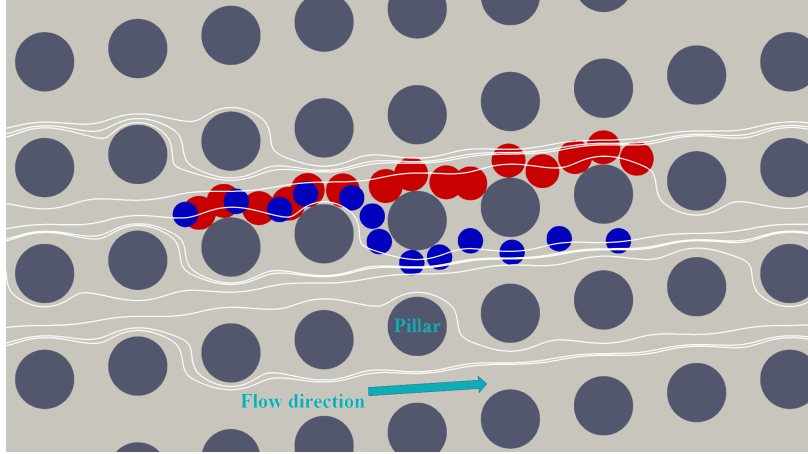


Figure 11: DLD principle: small particles whose sizes are less than the critical diameter follow the initial streamline and move in a zigzag direction (blue), while large particles travel in bumping mode (red) and move to the next streamline, where white streamlines of fluid flow are shown in the background.

to solve for a unified variable pair of velocity and pressure defined only on the background (Eulerian) fluidic mesh nodes in the entire domain. We further design advanced numerical implementation algorithms to deal with the structural collision by means of a fixed-point nonlinear iteration, to solve the developed nonlinear finite element approximation system by Newton’s linearization, and to handle the interpolation process between the background Eulerian fluidic mesh and the foreground updated-Lagrangian structural mesh through elemental computations and numerical quadrature points in an elementwise manner. Our proposed numerical methods are validated through two benchmark problems, self-designed and physically designed microfluidic DLD problems, respectively, by checking numerical convergence rates and/or comparing with benchmark/physical experimental results, which all return good agreements. Numerical simulations carried out by the developed unified-field, monolithic fictitious domain-based mixed finite element method (UFMFD-FEM) can help to optimize the design of cascaded filter DLD microchips in an accurate and efficient fashion for the sake of practically isolating circulating tumor cells from blood cells in the blood fluid.

We will extend our numerical study to a rigorous theoretical analysis of the proposed UFMFD-FEM in our next work as indicated in Remark 4.1. In addition, in our next paper we will also develop more advanced numerical algorithms for the proposed UFMFD-FEM on the aspect of efficiency improvement, such as the domain decomposition method (DDM), the adaptive time-step method, the locally adaptive mesh refinement method, as well as the multi-timescale approach. On the other hand, we will investigate a possible dimension error brought by the two-dimensional FSCI simulation on an actually three-dimensional DLD microchip whose thickness (about  $30 \mu\text{m}$ ) is relatively thin though, by doing 3D simulations for more realistic DLD problems since our developed FSCI modeling approach can be seamlessly extended to high dimensions. Moreover, we will conduct more in-depth studies on the modeling of structural collisions and its numerical techniques in more accurate and robust manner, and investigate more complicated cases of collision effects amongst multiple particles that is beyond the current contact phenomenon in this paper between a single particle and the fluidic channel wall.

## Acknowledgments

C. Wang was supported by National Natural Science Foundation of China grant (No. 12171366), P. Sun was partially supported by a grant from the Simons Foundation (MPS-706640), J. Xu was supported in part by KAUST Baseline Research Fund.

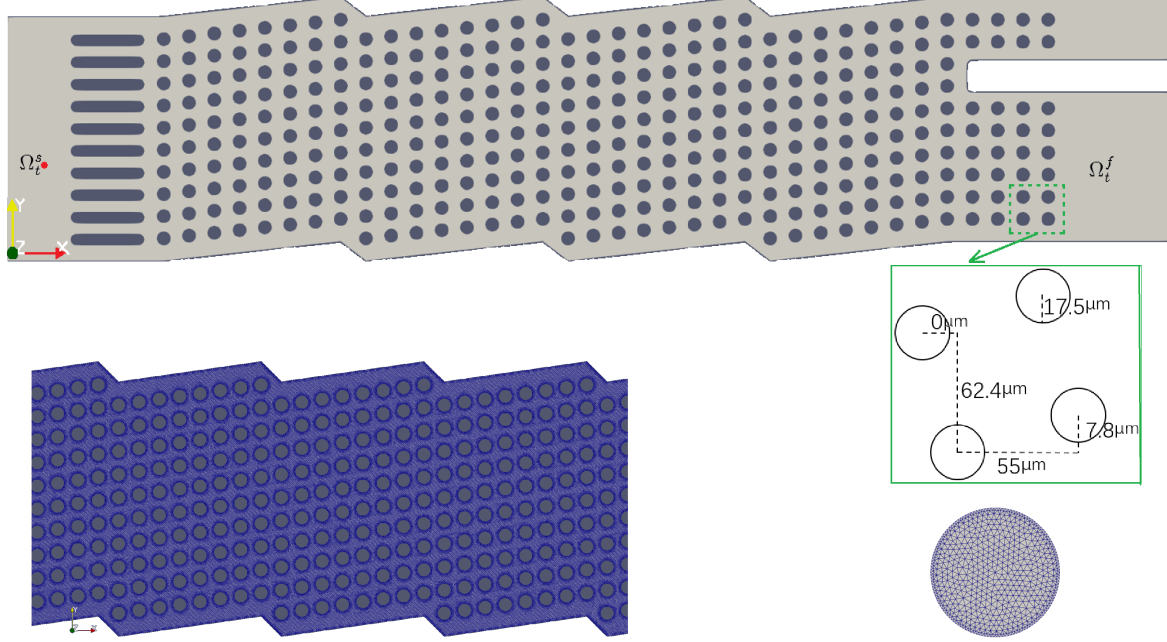


Figure 12: Computational domain of the FSI problem in a DLD microchip (top), a portion of its mesh triangulation (bottom left), and the structural mesh (bottom right).

## Appendix A. Description of interpolation process between fluidic and structural meshes

In this appendix, we give a detailed implementation description for the interpolation-related inner product terms arising from the developed UFMFD-FEM which occur in the structural domain  $\Omega_s^t$  associated with its triangulation  $\mathcal{T}_{h_s}^t$  ( $t \in (0, T]$ ) and whose integrand functions involve the mesh-dependent trial function  $\mathbf{v}_h \in \mathbf{V}_h$  and/or its test function  $\tilde{\mathbf{v}}_h \in \mathbf{V}_{0,h}$  that are associated with the fixed background fluidic mesh  $\mathcal{T}_h$ . To conveniently describe the interpolation procedure for inner products over two overlapped meshes  $\mathcal{T}_h$  and  $\mathcal{T}_{h_s}^t$ , without loss of generality, we only consider the following two general terms in the form of

$$(u, v)_{\Omega_s^t} \quad \text{and} \quad (\nabla u, \nabla v)_{\Omega_s^t}, \quad (\text{A.1})$$

where  $u$  and  $v$  are two general finite element functions associated with  $\mathcal{T}_h = \bigcup_{i=1}^M e_{f,i}$  and  $\mathcal{T}_{h_s}^t = \bigcup_{i=1}^{M_s} e_{s,i}^t$ , respectively. Thus, the two terms in (A.1) can be rewritten as

$$\sum_{i=1}^{M_s} (u, v)_{e_{s,i}^t} \quad \text{and} \quad \sum_{i=1}^{M_s} (\nabla u, \nabla v)_{e_{s,i}^t}. \quad (\text{A.2})$$

Moreover, if we adopt the following quadrature scheme with  $N_q$  quadrature points  $\{\hat{\mathbf{x}}_j\}_{j=1}^{N_q}$  defined in an element  $\hat{e}$ ,

$$\int_{\hat{e}} \hat{f}(\hat{\mathbf{x}}) d\hat{\mathbf{x}} \approx \sum_{j=1}^{N_q} \omega_j \hat{f}(\hat{\mathbf{x}}_j),$$

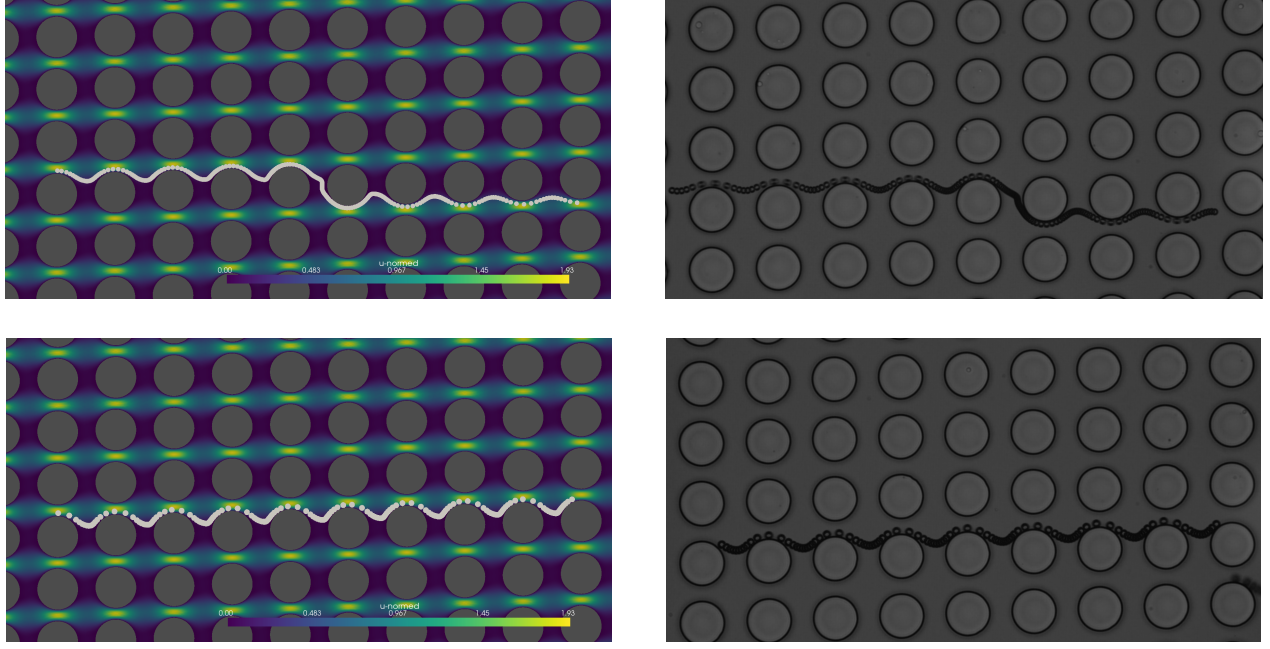


Figure 13: Comparisons of the lateral migration of particles between numerical (**left column**) and physical (**right column**) experiments for the diameter of particle  $D=4$  (**top row**) and  $D=5$  (**bottom row**), which illustrate that both numerical and physical results show the same critical diameter  $D_c \in (4, 5)$ .

then we can approximate two inner product terms in (A.1) as follows,

$$\begin{aligned} (u, v)_{\Omega_s^t} &= \sum_{i=1}^{M_s} \sum_{j=1}^{N_q} \omega_j u(\mathbf{x}_{ij}) v(\mathbf{x}_{ij}), \\ (\nabla u, \nabla v)_{\Omega_s^t} &= \sum_{i=1}^{M_s} \sum_{j=1}^{N_q} \omega_j \nabla u(\mathbf{x}_{ij}) \nabla v(\mathbf{x}_{ij}), \end{aligned}$$

where  $\mathbf{x}_{ij}$  denotes the coordinate of the  $j$ -th quadrature point  $\hat{\mathbf{x}}_j$  in the  $i$ -th structural element  $e_{s,i}^t$ .

Note that  $v(\mathbf{x})$  is defined on  $\mathcal{T}_{h_s}^t$ , which implies that  $v(\mathbf{x}_{ij})$  and  $\nabla v(\mathbf{x}_{ij})$  can be computed by the following isoparametric transformations,

$$v(\mathbf{x}_{ij}) = \sum_{m=1}^{N_{s,p}} v_{i,m} \psi_{i,m}(\mathbf{x}_{ij}), \quad \nabla v(\mathbf{x}_{ij}) = \sum_{m=1}^{N_{s,p}} v_{i,m} \nabla \psi_{i,m}(\mathbf{x}_{ij}), \quad (\text{A.3})$$

where  $\{\psi_{i,m}\}_{m=1}^{N_{s,p}}$  are  $N_{s,p}$  nodal basis functions in the structural element  $e_{s,i}^t \subset \mathcal{T}_{h_s}^t$ , and, the restriction of  $v$  in  $e_{s,i}^t$  is denoted by  $\sum_{m=1}^{N_{s,p}} v_{i,m} \psi_{i,m}$ . On the other hand, we use the following three steps to compute  $u(\mathbf{x}_{ij})$  and  $\nabla u(\mathbf{x}_{ij})$ : (i) for each quadrature point  $\mathbf{x}_{ij}$  ( $i = 1, \dots, M_s$ ,  $j = 1, \dots, N_q$ ), we find the (first) fluidic element  $e_{f,k_{ij}} \subset \mathcal{T}_h$  that contains the quadrature point  $\mathbf{x}_{ij}$ . Note that the element in  $\mathcal{T}_h$  that contains  $\mathbf{x}_{ij}$  may be more than one in the sense that  $\mathbf{x}_{ij}$  coincides with the vertices of  $\mathcal{T}_h$ ; (ii) Let  $\{\phi_{k_{ij},l}\}_{l=1}^{N_{f,p}}$  be  $N_{f,p}$  nodal basis functions in the fluidic element  $e_{f,k_{ij}} \subset \mathcal{T}_h$ . The values of  $\phi_{k_{ij},l}(\mathbf{x}_{ij})$  and  $\nabla \phi_{k_{ij},l}(\mathbf{x}_{ij})$  can also be computed by an isoparametric transformation, where the reference element  $\hat{e}_{f,k_{ij}}$  of  $e_{f,k_{ij}}$  is used and the reference quadrature point of  $\mathbf{x}_{ij}$  in  $\hat{e}_{f,k_{ij}}$  is computed; (iii) the

desired values,  $u(\mathbf{x}_{ij})$  and  $\nabla u(\mathbf{x}_{ij})$ , are computed by

$$u(\mathbf{x}_{ij}) = \sum_{l=1}^{N_{f,p}} u_{k_{ij},l} \phi_{k_{ij},l}(\mathbf{x}_{ij}), \quad \nabla u(\mathbf{x}_{ij}) = \sum_{l=1}^{N_{f,p}} u_{k_{ij},l} \nabla \phi_{k_{ij},l}(\mathbf{x}_{ij}), \quad (\text{A.4})$$

where the restriction of  $u$  in  $e_{f,k_{ij}} \subset \mathcal{T}_h$  is denoted by  $\sum_{l=1}^{N_{f,p}} u_{k_{ij},l} \phi_{k_{ij},l}$ .

Therefore, we have

$$(u, v)_{\Omega_s^t} = \sum_{i=1}^{M_s} \sum_{j=1}^{N_q} \sum_{l=1}^{N_{f,p}} \sum_{m=1}^{N_{s,p}} \omega_j u_{k_{ij},l} v_{i,m} \phi_{k_{ij},l}(\mathbf{x}_{ij}) \psi_{i,m}(\mathbf{x}_{ij}), \quad (\text{A.5})$$

$$(\nabla u, \nabla v)_{\Omega_s^t} = \sum_{i=1}^{M_s} \sum_{j=1}^{N_q} \sum_{l=1}^{N_{f,p}} \sum_{m=1}^{N_{s,p}} \omega_j u_{k_{ij},l} v_{i,m} \nabla \phi_{k_{ij},l}(\mathbf{x}_{ij}) \nabla \psi_{i,m}(\mathbf{x}_{ij}). \quad (\text{A.6})$$

where the element index  $k_{ij}$  of  $\mathcal{T}_h$  depends on the structural element index  $i$  of  $\mathcal{T}_{h_s}^t$  and on the quadrature point index  $j$ . We remark that  $k_{ij}$  may take different values even for the cases that the element index  $i$  is the same but the quadrature point index  $j$  is different.

Furthermore, to compute and assemble the elementwise finite element matrix, we only need to take  $v = \psi_{i,m}$  as the test function in (A.1). Thus, (A.5) and (A.6) can be further simplified as

$$(u, v)_{\Omega_s^t} = \sum_{i=1}^{M_s} \sum_{j=1}^{N_q} \sum_{l=1}^{N_{f,p}} \omega_j u_{k_{ij},l} \phi_{k_{ij},l}(\mathbf{x}_{ij}) \psi_{i,m}(\mathbf{x}_{ij}), \quad (\text{A.7})$$

$$(\nabla u, \nabla v)_{\Omega_s^t} = \sum_{i=1}^{M_s} \sum_{j=1}^{N_q} \sum_{l=1}^{N_{f,p}} \omega_j u_{k_{ij},l} \nabla \phi_{k_{ij},l}(\mathbf{x}_{ij}) \nabla \psi_{i,m}(\mathbf{x}_{ij}), \quad (\text{A.8})$$

for  $m = 1, \dots, N_{s,p}$ , where  $u_{k_{ij},l}$  is called the degree of freedoms (DOFs) defined on the vertices of  $\mathcal{T}_h$ .

## References

- [1] P. Alart and A. Curnier. A mixed formulation for frictional contact problems prone to Newton like solution methods. *Computer Methods in Applied Mechanics and Engineering*, 92:553–375, 1991.
- [2] M. Amabili. *Hyperelasticity of Soft Biological and Rubber Materials*, pages 151–224. Cambridge University Press, 2018.
- [3] F. Auricchio, D. Boffi, L. Gastaldi, A. Lefieux, and A. Reali. On a fictitious domain method with distributed Lagrange multiplier for interface problems. *Applied Numerical Mathematics*, 95:36–50, 2015.
- [4] I. Babuška. Error-bounds for finite element method. *Numerische Mathematik*, 16(4):322–333, 1971.
- [5] D. Boffi and L. Gastaldi. A fictitious domain approach with Lagrange multiplier for fluid-structure interactions. *Numerische Mathematik*, 135:711–732, 2017.
- [6] D. Boffi, L. Gastaldi, and M. Ruggeri. Mixed formulation for interface problems with distributed lagrange multiplier. *Computers & Mathematics with Applications*, 68:2151–2166, 2014.
- [7] M. Braack, E. Burman, V. John, and G. Lube. Stabilized finite element methods for the generalized Oseen problem. *Computer Methods in Applied Mechanics and Engineering*, 196(4):853–866, 2007.
- [8] F. Brezzi. On the existence, uniqueness and approximation of saddle point problems arising from Lagrangian multipliers. *RAIRO Analyse Numerique*, 8:129–151, 1974.

- [9] S. K. Chakrabarti, editor. *Numerical Models in Fluid Structure Interaction, Advances in Fluid Mechanics*, volume 42. WIT Press, 2005.
- [10] F. Chouly and P. Hild. A nitsche-based method for unilateral contact problems: Numerical analysis. *SIAM Journal on Numerical Analysis*, 51(2):1295–1307, 2013.
- [11] E. H. Dowell and K. C. Hall. Modeling of fluid-structure interaction. *Annu. Rev. Fluid Mech.*, 33:445–490, 2001.
- [12] L. Franca and T.J.R. Hughes. Convergence analyses of Galerkin least-squares methods for symmetric advective-diffusive forms of the Stokes and incompressible Navier-Stokes equations. *Comput. Methods Appl. Mech. Eng.*, 105:285–298, 1993.
- [13] L. Gastaldi. A priori error estimates for the arbitrary Lagrangian Eulerian formulation with finite elements. *J. Numer. Math.*, 9:123–156, 2001.
- [14] R. Glowinski, T.-W. Pan, T.I. Hesla, and D.D. Joseph. A distributed Lagrange multiplier/fictitious domain method for particulate flows. *Int. J. Multiphase Flow*, 25:755–794, 1999.
- [15] R. Glowinski, T.-W. Pan, T.I. Hesla, D.D. Joseph, and J. P eriaux. A fictitious domain approach to the direct numerical simulation of incompressible viscous flow past moving rigid bodies: Application to particulate flow. *J. Comput. Phys.*, 169:363–426, 2001.
- [16] P. Grisvard. *Elliptic problems in nonsmooth domains, in: Monographs and Studies in Mathematics*, volume 24. Pitman (Advanced Publishing Program), Boston, MA, USA, 1985.
- [17] W. Han, F. Jing, and Y. Yao. Stabilized mixed finite element methods for a Navier–Stokes hemivariational inequality. *BIT Numerical Mathematics*, 63:46, 2023.
- [18] W. Hao, P. Sun, J. Xu, and L. Zhang. Multiscale and monolithic arbitrary Lagrangian-Eulerian finite element method for a hemodynamic fluid-structure interaction problem involving aneurysms. *Journal of Computational Physics*, 433:110181, 2021.
- [19] C. W. Hirt, A. A. Amsden, and J. L. Cook. An arbitrary Lagrangian-Eulerian computing method for all flow speeds. *J. Comput. Phys.*, 14:227–253, 1974.
- [20] H. H. Hu. Direct simulation of flows of solid-liquid mixtures. *Int. J. Multiphase Flow*, 22:335–352, 1996.
- [21] L. R. Huang, E. C. Cox, R. H. Austin, and J. C. Sturm. Continuous particle separation through deterministic lateral displacement. *Science*, 304(5673):987–990, 2004.
- [22] A. Huerta and W.K. Liu. Viscous flow structure interaction. *Trans. ASME J. Pressure Vessel Technol.*, 110:15–21, 1988.
- [23] T. Hughes, L. Franca, and M. Balestra. A new finite element formulation for computational fluid dynamics: V. circumventing the Babuska-Brezzi condition: a stable Petrov-Galerkin formulation of the Stokes problem accommodating equal-order interpolations. *Comput. Meth. Appl. Mech. Engrg.*, 59(1):85–99, 1986.
- [24] T.J.R. Hughes, W.K. Liu, and T.K. Zimmermann. Lagrangian-Eulerian finite element formulation for incompressible viscous flows. *Comput. Methods Appl. Mech. Eng.*, 29:329–349, 1981.
- [25] T. Inamuro, K. Maeba, and F. Ogino. Flow between parallel walls containing the lines of neutrally buoyant circular cylinders. *Int. J. Multiphase Flow*, 26:1981, 2000.
- [26] G. B. Jeffery. The motion of ellipsoidal particles immersed in a viscous fluid. *Proceedings of the Royal Society of London. Series A, Containing papers of a mathematical and physical character*, 102(715):161–179, 1922.

- [27] A. A. Johnson and T. E. Tezduyar. 3D simulation of fluid-particle interactions with the number of particles reaching 100. *Comput. Methods Appl. Mech. Eng.*, 145:301–321, 1997.
- [28] R. J. LeVeque and Z. Li. The immersed interface method for elliptic equations with discontinuous coefficients and singular sources. *SIAM J. Numer. Anal.*, 31:1019–1044, 1994.
- [29] Z. Li and M.-C. Lai. The immersed interface method for the Navier-Stokes equations with singular forces. *J. Comput. Phys.*, 171:822–842, 2001.
- [30] M. Ling, W. Han, and S. Zeng. A pressure projection stabilized mixed finite element method for a Stokes hemivariational inequality. *Journal of Scientific Computing*, 92:13, 2022.
- [31] W. K. Liu, D. W. Kim, and S. Tang. Mathematical foundations of the immersed finite element method. *Comput. Mech.*, 39:211–222, 2006.
- [32] W. K. Liu, Y. Liu, D. Farrell, L. Zhang, X. Wang, Y. Fukui, N. Patankar, Y. Zhang, C. Bajaj, X. Chen, and H. Hsu. Immersed finite element method and its applications to biological systems. *Comput. Methods Appl. Mech. Engrg.*, 195:1722–1749, 2006.
- [33] X. Liu and S. Li. A variational multiscale stabilized finite element method for the Stokes flow problem. *Finite Elements in Analysis and Design*, 42:580–591, 2006.
- [34] V. R. Loon. *A 3D method for modelling the fluid-structure interaction of heart valves*. Eindhoven: Technische Universiteit Eindhoven, DOI: 10.6100/IR594604, 2005.
- [35] A. Lundberg, P. Sun, and C. Wang. Distributed Lagrange multiplier-fictitious domain finite element method for Stokes interface problems. *International Journal of Numerical Analysis & Modeling*, 16:939–963, 2019.
- [36] H. J.-P. Morand and R. Ohayon. *Fluid-Structure Interaction: Applied Numerical Methods*, volume 42. Wiley, 1995.
- [37] R. Nemer, A. Larcher, T. Coupez, and E. Hachem. Stabilized finite element method for incompressible solid dynamics using an updated Lagrangian formulation. *Comput. Methods Appl. Mech. Engrg.*, 384:113923, 2021.
- [38] C. Nitikitpaiboon and K.J. Bathe. An arbitrary Lagrangian-Eulerian velocity potential formulation for fluid-structure interaction. *Comput. Struct.*, 47:871–891, 1993.
- [39] F. Nobile and L. Formaggia. A Stability Analysis for the Arbitrary Lagrangian Eulerian Formulation with Finite Elements. *East-West Journal of Numerical Mathematics*, 7:105–132, 2010.
- [40] E. Onáte, J. Garcia, and S. Idelsohn. Computation of the stabilization parameter for the finite element solution of advective-diffusive problems. *Int. J. Numerical Methods Fluids*, 25:1385–1407, 1997.
- [41] T.-W. Pan and R. Glowinski. Direct simulation of the motion of neutrally buoyant circular cylinders in plane Poiseuille flow. *Journal of Computational Physics*, 181:260–279, 2002.
- [42] T.-W. Pan, S. Zhao, X. Niu, and R. Glowinski. A DLM/FD/IB method for simulating compound vesicle motion under creeping flow condition. *Journal of Computational Physics*, 300:241–253, 2015.
- [43] C. S. Peskin. Flow patterns around heart valves: a numerical method. *J. Comput. Phys.*, 10:252–271, 1972.
- [44] C. S. Peskin. The immersed boundary method. *Acta numerica*, 11:479–517, 2002.
- [45] C. S. Peskin and Be. F. Printz. Improved volume conservation in the computation of flows with immersed elastic boundaries. *Journal of computational physics*, 105(1):33–46, 1993.
- [46] J. H. Seo, V. Vedula, T. Abraham, and R. Mittal. Multiphysics computational models for cardiac flow and virtual cardiography. *Int. J. Numer. Meth. Biomed. Engrg.*, 29:850–869, 2013.

- [47] X. Shi and N. Phan-Thien. Distributed Lagrange multiplier/fictitious domain method in the framework of lattice Boltzmann method for fluid-structure interactions. *J. Comput. Phys.*, 206:81–94, 2005.
- [48] J. C. Simo and T. A. Laursen. An augmented Lagrangian treatment of contact problems involving friction. *Computers & Structures*, 42:97–116, 1992.
- [49] M. Souli and D. J. Benson, editors. *Arbitrary Lagrangian Eulerian and Fluid-Structure Interaction: Numerical Simulation*. Wiley-ISTE, 2010.
- [50] P. Sun. Fictitious domain finite element method for Stokes/elliptic interface problems with jump coefficients. *Journal of Computational and Applied Mathematics*, 356:81–97, 2019.
- [51] P. Sun and C. Wang. Fictitious domain finite element method for Stokes/parabolic interface problems with jump coefficients. *Applied Numerical Mathematics*, 152:199–220, 2020.
- [52] K Takizawa, B. Henicke, T. E. Tezduyar, M. Hsu, and Y. Bazilevs. Stabilized space-time computation of wind-turbine rotor aerodynamics. *Computational Mechanics*, 48:333–344, 2011.
- [53] Z. Tan, K.M. Lim, and B.C. Khoo. An immersed interface method for Stokes flows with fixed/moving interfaces and rigid boundaries. *J. Comput. Phys.*, 228:6855–6881, 2009.
- [54] T. E. Tezduyar. Stabilized finite element formulations for incompressible flow computations. *Adv. Appl. Mech.*, 28:1–44, 1992.
- [55] C. Wang and P. Sun. A fictitious domain method with distributed Lagrange multiplier for parabolic problems with moving interfaces. *Journal of Scientific Computing*, 70:686–716, 2017.
- [56] C. Wang and P. Sun. An augmented Lagrangian Uzawa iterative method for solving double saddle-point systems with semi-definite (2,2) block and its application to DLM/FD method for elliptic interface problems. *Communications in Computational Physics*, 30:124–143, 2021.
- [57] C. Wang, P. Sun, H. Shi, R. Lan, and F. Xu. Effects of numerical integration on DLM/FD method for solving interface problems with body-unfitted meshes. *Springer Lecture Notes in Computer Science*, 11539:551–567, 2019.
- [58] X. Wang. From immersed boundary method to immersed continuum method. *International Journal for Multiscale Computational Engineering*, 4:127–145, 2006.
- [59] Y. Wang, P. K. Jimack, and M. A. Walkley. A one-field monolithic fictitious domain method for fluid-structure interactions. *Computer Methods in Applied Mechanics and Engineering*, 317:1146–1168, 2017.
- [60] P. N. Watton, X. Y. Luo, X. Wang, G. M. Bernacca, P. Molloy, and D. J. Wheatley. Dynamic modelling of prosthetic chorded mitral valves using the immersed boundary method. *Journal of Biomechanics*, 40:613–626, 2007.
- [61] K. Yang, P. Sun, L. Wang, J. Xu, and L. Zhang. Modeling and simulation for fluid-rotating structure interaction. *Comput. Methods Appl. Mech. Engrg.*, 311:788–814, 2016.
- [62] Z. Yu. A DLM/FD method for fluid/flexible-body interactions. *J. Comput. Phys.*, 207:1–27, 2005.
- [63] Z. Yu, N. Phan-Thien, and R.I. Tanner. Dynamic simulation of sphere motion in a vertical tube. *J. Fluid Mech.*, 518:61–93, 2004.
- [64] L. Zhang, A. Gerstenbetger, X. Wang, and W.K. Liu. Immersed finite element method. *Comput. Methods Appl. Mech. Eng.*, 193:2051–2067, 2004.
- [65] L. T. Zhang and M. Gay. Immersed finite element method for fluid-structure interactions. *J. Fluids Struct.*, 23:839–857, 2007.
- [66] L. T. Zhang and M. Gay. Imposing rigidity constraints on immersed objects in unsteady fluid flows. *Comput. Mech.*, 42:357–370, 2008.